Research Square

Preprints are preliminary reports that have not undergone peer review.
They should not be considered conclusive, used to inform clinical practice,
or referenced by the media as validated information.

Continuous-wave instabilities and multi-pulse structures in a complex Ginzburg-Landau equation with a power-law nonlinearity of arbitrary order

Peguy Kameni Nteutse

peguy.kameni@aims.ac.rw

African Institute for Mathematical Sciences

Research Article

Keywords:

Posted Date: October 30th, 2026

DOI: https://doi.org/10.21203/rs.3.rs-11550884/v1

License: This work is licensed under a Creative Commons Attribution 4.0 International License.
Read Full License

Additional Declarations: No competing interests reported.

Continuous-wave instabilities and multi-pulse structures in a complex Ginzburg-Landau equation with a power-law nonlinearity of arbitrary order

Peguy Kameni Nteutse[1]

[1]African Institute for Mathematical Sciences (AIMS), 17 KN 16 Ave, Nyarugenge District -Kigali, P.O Box, 7150, Kigali, Rwanda

Corresponding Author: peguy.kameni@aims.ac.rw, peguykameni72@gmail.com

Abstract

We study a generalized complex Ginzburg–Landau equation with linear gain, spectral filtering, dispersion and a power-law nonlinearity of arbitrary order γ, which describes laser propagation in media with Kerr ($\gamma = 2$) and higher-order non-Kerr nonlinearities. A travelling-wave reduction yields a three-dimensional dynamical system whose singular points are the continuous waves (CWs). For any γ, the CWs lie on a universal locus fixed by the gain and γ, inside a frequency band whose edges do not depend on γ. We show that the linear stability problem of any CW maps exactly onto that of a plane wave of the cubic equation with an effective gain and an effective wavenumber. Consequently, the Benjamin–Feir–Newell condition $1 + \nu\mu < 0$ destabilizes all the CWs independently of γ, the growth rate of the zero-wavenumber CW scales as $\gamma - 1$, and the band of Eckhaus-stable wavenumbers widens with γ. In the unstable regime, numerical simulations of the reduced system with Luther's sixth-order Runge–Kutta scheme reveal stationary multi-pulse bursts with phase slips for a zero velocity, and periodic moving pulse trains, born on a stable limit cycle, for a nonzero velocity. In both cases, increasing γ clamps the pulse peaks and regularizes the dynamics.

Keywords: complex Ginzburg–Landau equation; power-law nonlinearity; continuous waves; modulational instability; Benjamin–Feir–Newell criterion; Eckhaus instability; absolute instability; multi-pulse bursts; modulated amplitude waves; phase slips.

1 Introduction

The complex Ginzburg–Landau (CGL) equation ranks among the most extensively investigated nonlinear evolution equations in physics. It arises as the universal amplitude equation of spatially extended systems in the vicinity of an oscillatory instability and, depending on how its coefficients are interpreted, it models phase transitions and superconductivity, convection and other hydrodynamic instabilities, oscillatory chemical reactions, Bose–Einstein condensates, and nonlinear electrical transmission lines [1–3]. In nonlinear optics, the CGL equation describes the slowly varying envelope of an optical field propagating through a medium in which linear gain or loss, spectral filtering, dispersion or diffraction, nonlinear refraction, and nonlinear absorption act simultaneously [4–6]. Since the response of optical media to the field intensity is not always cubic, the cubic equation has been extended along several lines, including cubic–quintic and higher-order nonlinearities [7, 8], power-law as well as dual- and triple-power-law self-phase modulation [9, 10], and multiphoton absorption of arbitrary order combined with non-Kerr refraction [11–15].

A key notion associated with the CGL equation is that of dissipative solitons [4, 5]. Unlike the solitons of conservative systems, which form continuous families maintained by a balance between dispersion and nonlinearity, dissipative solitons additionally require a balance between gain and loss. As a consequence, they exist only for isolated values of their parameters and behave as attractors of the dynamics [4, 16, 17]. Such localized structures, together with their bound states,

their breathing and exploding variants, and their multidimensional and vortex counterparts, have been reported in a wide range of optical systems [5, 6, 18]. These localized states are connected to the simplest solution of the CGL equation, namely the continuous wave (CW), through modulational instability (MI): a CW that is unstable with respect to long-wavelength modulations disintegrates into periodic patterns and pulse trains [19, 20]. Within the CGL framework, the MI of the zero-wavenumber CW is governed by the Benjamin–Feir–Newell criterion, CWs with a nonzero wavenumber undergo the Eckhaus instability, and beyond these thresholds the field may develop phase or defect turbulence [1, 21]. In the cubic equation, the nonlinear development of the Eckhaus instability is organized by modulated amplitude waves, i.e., spatially periodic travelling structures that mediate the transition from phase to defect chaos [22–24]. The stability of CWs is usually assessed by adding a weak perturbation to the CW, linearizing the equation, and solving a 2×2 eigenvalue problem for the sideband amplitudes; the real part of the eigenvalue, regarded as a function of the modulation frequency, yields the growth rate of the perturbation and the width of the unstable band [25, 26]. An alternative and complementary route consists in reducing the CGL equation, through a travelling-wave ansatz, to a low-dimensional dynamical system whose singular points correspond to the CWs and whose trajectories represent pulses, fronts, and multi-pulse structures [25, 27, 28], in the spirit of the classical analysis of the coherent structures of the CGL equation [29, 30]. The relationship between CW stability and pulse formation has been addressed in a number of studies. For instance, for the cubic–quintic CGL equation, it was demonstrated that low-amplitude CWs are always unstable, that high-amplitude CWs are stable only within certain parameter domains, and that the MI of CWs is linked to, yet not in one-to-one correspondence with, the existence of stable pulses; an unstable CW may therefore evolve into pulses, into another CW, or simply decay [25]. A universal CGL model with a saturable nonlinearity was reduced to a three-dimensional dynamical system whose singular points provided the CW loci and whose numerical simulation generated multi-pulse structures [27]; a similar amplitude–phase formulation was employed to describe soliton combs in Kerr optomechanical microresonators [28]. More recently, all CWs of a cubic CGL equation including nonlinear gradient terms were shown to be unstable and to evolve into plain or oscillatory solitons, pulse trains, and bound states [31]. For nonlinearities of power-law type, existing analyses have mainly focused on the construction of exact solitary waves, complemented by the MI dispersion relation of the zero-wavenumber CW [9, 10], whereas the MI of optical fields subject to multiphoton absorption of arbitrary order has been investigated in models coupled to an electron plasma [12, 14, 15]. Taken together, these studies show that CW stability determines whether, how rapidly, and on which scale a continuous optical field breaks up into pulses; CW stability is therefore the natural starting point of any analysis of pulse formation.

The CGL equation has also found valuable applications in laser dynamics [11–15, 27, 28]. In this field, it is used to model laser inscription in transparent media, a process in which a laser source irradiates a nonlinear transparent material and transfers its energy to it. This process holds considerable potential for technological applications such as laser drilling, cutting, welding, ablation, and surface texturing of materials [15]. To meet the precision requirements of the final product, two categories of laser sources are commonly employed, namely CW lasers and pulsed lasers. CW lasers typically deliver powers of the order of one to a few kilowatts, whereas pulsed lasers usually operate well below 1 kW but offer a broad range of wavelengths, pulse durations, and pulse repetition rates [11]. In addition to the extensive experimental research on laser interactions with transparent materials such as fused silica, theoretical efforts have been devoted to a deeper understanding of the fundamental mechanisms underlying the inscription process [11–13]. In particular, the dynamics of lasers propagating in transparent materials with either Kerr or non-Kerr optical nonlinearities has been examined in both the anomalous- and normal-dispersion regimes in [14, 15, 27].

The generalized CGL equation considered in this work, was studied by Doering *et al.* [16] for a nonlinearity of arbitrary order γ, and established the existence of global weak solutions in all spatial dimensions and for all nonlinearities, together with the existence of local strong solutions.

Their work constitutes a mathematical regularity theory, in which modulational instability enters only through the definiteness of the energy of the underlying NLS equation; it performs neither a linear stability analysis of the CWs of the dissipative equation itself nor numerical simulations. Further global-existence and stability results for generalized CGL equations were obtained more recently by Correia and Figueira [32]. In Ref. [1], Aranson and Kramer reviewed the cubic CGL equation, which corresponds to the model of Ref. [16] with $\gamma = 2$ and a unit gain $R = 1$, and its coherent structures in one, two and three dimensions, including the plane-wave solutions and their Benjamin–Feir–Newell and Eckhaus stability, the convective and absolute instabilities, holes, shocks, spirals, vortex filaments and spatio-temporal chaos. Their review is restricted to the cubic nonlinearity and its small quintic perturbations. General conditions for the stability of plane waves in CGL-type equations were also derived by Matkowsky and Volpert [33], without addressing the nonlinear structures that emerge from the instability. To the best of our knowledge, the role of the order γ of the nonlinearity in the dynamics of the field has therefore not been addressed systematically: Ref. [16] covers arbitrary γ but not the CWs and their instability, whereas Ref. [1] covers the CWs and their instability but only for $\gamma = 2$. The present work fills this gap. We show that, for any γ, the CWs lie on a universal locus fixed by the gain and γ, inside a frequency band whose edges do not depend on γ, and that high-order nonlinearities clamp their amplitudes close to unity. We also show that the linear stability problem of any CW maps exactly onto that of a plane wave of the cubic equation, with an effective gain and an effective wavenumber, which extends the Benjamin–Feir–Newell and Eckhaus criteria, as well as the classification into convective and absolute instabilities, to arbitrary γ. Finally, in the nonlinear regime, which is not covered by this mapping, we determine how γ shapes the stationary multi-pulse bursts ($v = 0$) and the periodic moving pulse trains ($v \neq 0$) of the reduced system; the latter are modulated amplitude waves of the type identified in the cubic equation [22, 23].

The remainder of the paper is organized as follows. Section 2 introduces the model and its reduction to a three-dimensional dynamical system. Section 3 is devoted to the singular solutions of this system, i.e., the CWs. In Sec. 4, the linear stability of the CWs is analysed: the Benjamin–Feir–Newell instability of the zero-wavenumber CW is studied in Sec. 4.1, the Eckhaus instability of the CWs with a nonzero wavenumber in Sec. 4.2, and the role of γ, together with the convective or absolute nature of the instability, in Sec. 4.3. In Sec. 5, the reduced system is integrated numerically with the sixth-order Runge–Kutta algorithm of Luther [34], first for stationary structures ($v = 0$, Sec. 5.1) and then for moving pulse trains ($v \neq 0$, Sec. 5.2). Finally, Sec. 6 summarizes the results and presents concluding remarks.

2 Model and its reduction to a three-dimensional dynamical system

We consider the spatio-temporal evolution of a complex field amplitude $A(t, z)$ in a one-dimensional, anisotropic, nonlinear dissipative medium with gain, diffusion (spectral filtering), dispersion, and an optical nonlinearity of arbitrary order. Since diffraction is neglected, the optical field propagates along a single spatial direction, here the z axis. Its dynamics is governed by the generalized complex Ginzburg–Landau (CGL) equation [16]:

$$\frac{\partial A}{\partial t} = RA + (1 + i\nu)\frac{\partial^2 A}{\partial z^2} - (1 + i\mu)|A|^{2(\gamma-1)}A, \tag{2.1}$$

where $A(t, z)$ is the complex optical field, z is the local spatial coordinate across the field, and t (in s) is the evolution time. The left-hand side of Eq. (2.1) describes the temporal evolution of the field. The first term on the right-hand side accounts for the linear amplification of the field, with a gain coefficient R (in s^{-1}) assumed to be positive. The second term combines two distinct linear processes. Its real part describes spectral filtering, and its imaginary part describes the group-velocity dispersion of the gain medium, with coefficient ν (in m^2, s^{-1}). The last term represents the nonlinear response of the medium. Its real part describes nonlinear saturation (nonlinear

damping), which balances the linear gain. Its imaginary part describes an intensity-dependent nonlinear frequency shift, whose strength is set by the dimensionless coefficient μ. This coefficient is measured relative to nonlinear saturation and may take any real value. The dimensionless parameter $\gamma > 1$ makes the nonlinear exponent $2(\gamma - 1)$ real and positive. It therefore fixes the order of the nonlinearity and thereby the type of nonlinearity prevailing in the active medium; for instance, $\gamma = 2$ corresponds to the cubic (Kerr-type) case and $\gamma = 3$ to the quintic case. In what follows, we take $\mu > 0$ and assume that the optical medium operates in the anomalous-dispersion regime, so that the dispersion coefficient ν is real and negative.

Equation (2.1) admits both CW and pulse solutions. To find them, we write the complex envelope $A(t, z)$ of the propagating optical field in terms of a real amplitude $a(t, z)$ and a real phase $\Phi(t, z)$, through the ansatz [28]

$$A(t, z) = a(t, z)\, e^{i(\Phi(t,z)-\omega t)}. \tag{2.2}$$

We then perform the Galilean transformation $\tau = z - vt$, which maps the dynamics from the space-time frame (t, z) onto a frame involving the single coordinate τ. Under this transformation, and after separation of the real and imaginary parts, the complex space-time partial differential equation (2.1) yields the following system of coupled second-order nonlinear ordinary differential equations for the real variables a and Φ:

$$\begin{cases} a'' + v\,a' - a\Phi'^2 - \nu(2a'\Phi' + a\Phi'') + R\,a - a^{2\gamma-1} = 0, \\ \nu(a'' - a\Phi'^2) + 2a'\Phi' + a\Phi'' + (v\Phi' + \omega)a - \mu\, a^{2\gamma-1} = 0. \end{cases} \tag{2.3}$$

Defining the instantaneous frequency as $M = \Phi'$ and the field transient as $y = a'$, where the primes denote derivatives with respect to τ, the system of two second-order Eqs. (2.3) ultimately leads to the following system of four coupled first-order nonlinear ordinary differential equations:

$$\begin{cases} a' = y, \qquad \Phi' = M, \\ y' = \dfrac{-v\,y + (1+\nu^2)aM^2 - (R + \nu(vM + \omega))a + (1 + \nu\mu)a^{2\gamma-1}}{1+\nu^2}, \\ M' = \dfrac{\nu v\,y - 2(1+\nu^2)yM + (\nu R - vM - \omega)a + (\mu - \nu)a^{2\gamma-1}}{(1+\nu^2)a}. \end{cases} \tag{2.4}$$

System (2.4) contains all the stationary and uniformly translating solutions of Eq. (2.1) [1, 30], with v and ω playing the role of eigenvalues: pulse solutions exist only for specific values of these parameters. In what follows, the singular points of this first-order system are determined first, and the system is then integrated numerically.

3 Singular solutions

For $v = 0$, the conditions $y = 0$, $y' = 0$ and $M' = 0$ [25], the singular solutions of the set of first-order nonlinear ordinary differential equations (2.4), i.e., its fixed points, are given by the roots of the two nonlinear equations

$$M_s^2 - \frac{R + \nu\omega}{1+\nu^2} + \frac{1+\nu\mu}{1+\nu^2}\, a_s^{2\gamma-2} = 0, \tag{3.1}$$

$$\omega - \nu R - (\mu - \nu)a_s^{2\gamma-2} = 0. \tag{3.2}$$

It is quite remarkable that Eq. (3.2) does not contain M_s; it directly relates the amplitude and the frequency of the CW. Substituting Eq. (3.2) into Eq. (3.1) yields

$$M_s^2 = R - a_s^{2\gamma-2}. \tag{3.3}$$

Physically, Eq. (3.3) shows that the stationary instantaneous frequency is not arbitrary but is constrained by the balance between the linear gain and the nonlinear contribution associated with the stationary field amplitude. Specifically, the gain coefficient R and the nonlinear exponent γ, together with the amplitude a_s, determine the magnitude of the stationary instantaneous frequency M_s, provided that $R \geq a_s^{2\gamma-2}$. The equation therefore establishes a direct relationship between the stationary amplitude and frequency, but fixes only M_s^2: each admissible amplitude corresponds to two CWs with opposite wavenumbers $\pm|M_s|$. For $\mu \neq \nu$, Eqs. (3.2) and (3.3) then give

$$(a_s,\, y_s,\, M_s) = \left(\left[\frac{\omega - \nu R}{\mu - \nu}\right]^{\frac{1}{2(\gamma-1)}},\ 0,\ \pm\sqrt{\frac{\mu R - \omega}{\mu - \nu}} \right). \tag{3.4}$$

Equation (3.4) gives the coordinates of the fixed points of system (2.4) in the (a, y, M) phase space for a prescribed frequency ω. These fixed points exist if and only if

$$\nu R < \omega \leq \mu R. \tag{3.5}$$

Eliminating the amplitude a_s between Eqs. (3.2) and (3.3), instead of the frequency ω, gives the dispersion relation of the CWs,

$$\omega = \mu R + (\nu - \mu) M_s^2, \tag{3.6}$$

which assigns a frequency to each admissible wavenumber M_s. This relation does not depend on γ. Setting $M_s = 0$ in Eqs. (3.3) and (3.6) gives the equilibrium amplitude and the frequency of the zero-wavenumber CW as

$$a_s = a_0 = R^{\frac{1}{2(\gamma-1)}}, \qquad \omega_0 = \mu R. \tag{3.7}$$

This corresponds to the exact balance $R\, a_0 = a_0^{2\gamma-1}$ between the linear gain and the nonlinear loss, as can be checked directly in system (2.3), while the frequency $\omega_0 = \mu R$ is the nonlinear frequency shift $\mu a_0^{2\gamma-2}$ induced by this amplitude.

Figure 1 illustrates the stationary solutions (3.3) in the (a, M) plane obtained for four different values of γ, namely $\gamma = 2, 3, 4, 5$, and for $0 < a \leq a_0$. We have chosen ν to be negative since, as shown below, the anomalous-dispersion regime $\nu < 0$ is the one in which the CWs can become modulationally unstable and break up into pulses. The other characteristic parameters of the model are given in the figure captions. Because it results from the elimination of ω in Eq. (3.1), the locus gathers all the nontrivial CWs, and it depends only on R and γ: the dispersive and nonlinear phase coefficients ν and μ do not modify the set of admissible (amplitude, wavenumber) pairs; they only assign a frequency to each pair through Eq. (3.6). Each curve decreases monotonically from $|M| = \sqrt{R}$ at $a \to 0$ to the zero-wavenumber CW $(a_0, 0)$, and the locus is symmetric with respect to $M = 0$; for $\gamma = 2$ it reduces to the circular arc $M^2 + a^2 = R$. A frequency ω inside the band (3.5) selects two CWs of equal amplitude and opposite wavenumbers $\pm M_s$ (squares); they merge at $(a_0, 0)$ when $\omega \to \mu R$ and reach the trivial state when $\omega \to \nu R$. Increasing R enlarges the existence domain in both directions. Increasing γ has a qualitatively different effect: since $a^{2\gamma-2}$ is negligible for $a < 1$ when γ is large, the curves stay close to $|M| = \sqrt{R}$ over most of the amplitude range and drop abruptly near a_0, and $a_0 \to 1$ as γ gets stronger. A high-order nonlinearity therefore acts as an almost hard intensity clamp: the nonlinear loss is inactive below $a \simeq 1$ and becomes dominant just above it, so that the CW amplitudes are confined close to unity whatever the gain.

Figure 2 shows the same CWs in the (ω, a) plane, from Eq. (3.2). For $\mu > \nu$ and $\gamma = 2, 3, 4, 5$, ω increases strictly with a, so that each curve rises without fold from the trivial state $(\nu R, 0)$ to $(\mu R, a_0)$: each frequency selects a unique CW amplitude, shared by the two wavenumbers $\pm M_s$. The band (3.5), of width $|\mu - \nu| R$ ($[-1, 3]$ for $R = 2$, shaded), grows linearly with the gain and with the mismatch between the nonlinear and dispersive coefficients, and its edges do not depend on γ. Only the band for $R = 2$ is shaded, which is the gain used for the selected pair at ω^* in Fig. 1 and in

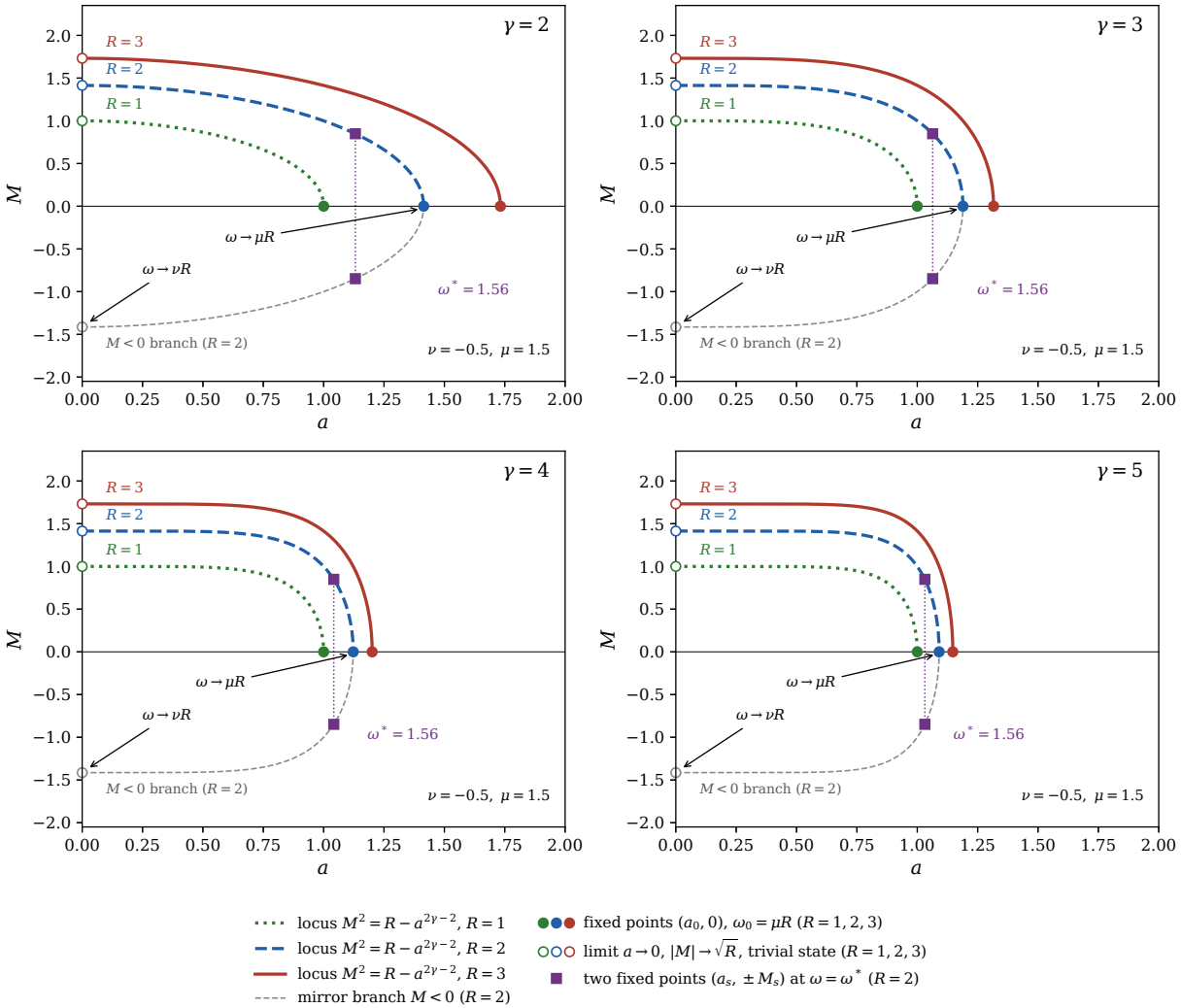


Figure 1: Locus of the CW singular points in the (a, M) plane, Eq. (3.3), for $\gamma = 2, 3, 4, 5$ and $R = 1$ (dotted), $R = 2$ (dashed) and $R = 3$ (solid); $\nu = -0.5$, $\mu = 1.5$. The thin grey dashed curve is the branch $M < 0$ for $R = 2$. Filled circles: zero-wavenumber CWs $(a_0, 0)$; open circles: limit $a \to 0$, $|M| \to \sqrt{R}$; squares: the pair $(a_s, \pm M_s)$ selected by $\omega^* = 1.56$ for $R = 2$. The frequency ω varies along each curve.

the stability analysis of Sec. 4. For $\nu < 0 < \mu$, the bands obtained for $R = 1$ and $R = 3$, $]-0.5, 1.5]$ and $]-1.5, 4.5]$, are nested with it and follow from it by the dilation $\omega \to \omega R/2$, so that shading them would only obscure the curves. The lower edge νR is negative because the system operates in the focusing regime $\nu < 0 < \mu$: according to Eq. (3.6), the frequency of low-amplitude CWs is dominated by the dispersive contribution νM^2, while that of high-amplitude CWs is dominated by the nonlinear contribution $\mu a^{2\gamma-2}$. The order of the nonlinearity only reshapes the curves within this fixed band: for $\gamma = 2$ the intensity a^2 grows linearly with ω, whereas for large γ the amplitude rises almost vertically just above νR and then saturates, so that most of the band is occupied by CWs of nearly unit amplitude. In summary, the existence domain of the CWs is controlled by R (size), by ν and μ (frequency band) and by γ (distribution of amplitudes within the band).

4 Modulational-instability analysis

We first analyse the modulational instability of the zero-wavenumber CW (Sec. 4.1), which is of Benjamin–Feir–Newell type, and then extend the analysis to the CWs with a nonzero wavenumber (Sec. 4.2), for which the modulational instability takes the form of the Eckhaus instability. In Sec. 4.3, we show that this reduction actually holds for any γ, after a rescaling of the gain and of

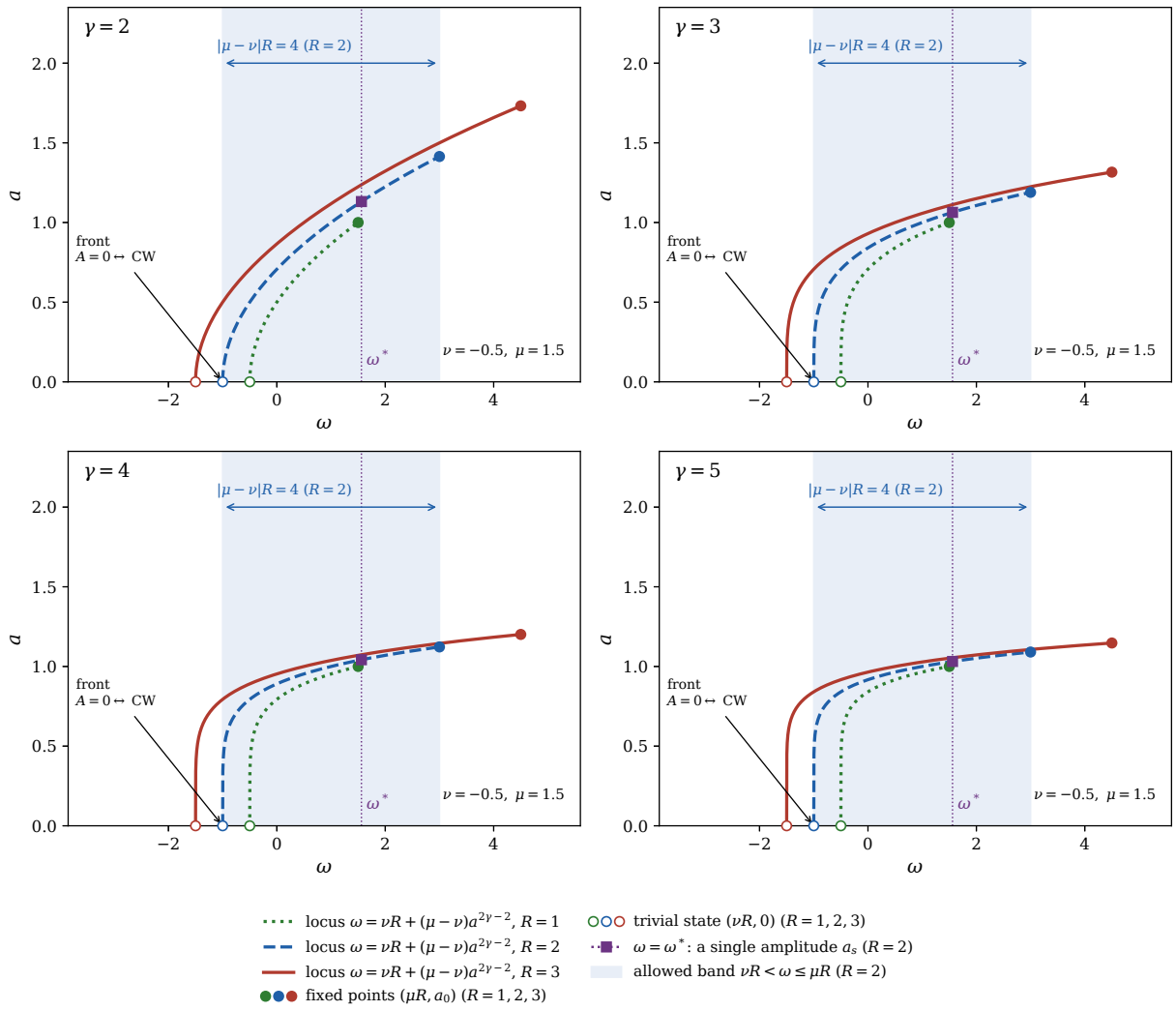


Figure 2: CW amplitude a versus frequency ω, Eq. (3.2), for $\gamma = 2, 3, 4, 5$ and $R = 1$ (dotted), $R = 2$ (dashed) and $R = 3$ (solid); $\nu = -0.5$, $\mu = 1.5$. Filled circles: $(\mu R, a_0)$; open circles: $(\nu R, 0)$; shaded region: existence band $\nu R < \omega \leq \mu R$ for $R = 2$; the vertical dotted line at $\omega^* = 1.56$ crosses the curve $R = 2$ at a single amplitude (square).

the wavenumber, and we use it to discuss the convective and absolute nature of the instability.

4.1 Benjamin–Feir–Newell instability of the zero-wavenumber CW

In the previous section, we determined the fixed-point solutions of the generalized CGL equation (2.1) in a stationary frame. These fixed points are singular solutions of the reduced system (2.4), and they describe the continuous waves (CWs) of the optical field: a_s is the CW amplitude and M_s its wavenumber (instantaneous frequency), given by Eqs. (3.1) and (3.2). Their existence and their positions in the (a, M) and (ω, a) planes depend strongly on the characteristic parameters of the model, namely the linear gain R, the coefficients ν and μ, and the order γ of the nonlinearity. To examine the stability of these singular solutions, we now study their response to harmonic modulations in space and time, within the framework of modulational-instability theory. Let (a_s, M_s) be a fixed point of Eqs. (3.1)–(3.2). The corresponding solution of Eq. (2.1) is the harmonic wave

$$A(z, t) = a_s \, e^{i(M_s z - \omega t)}, \tag{4.1}$$

where a_s is the amplitude of the harmonic wave, M_s its wavenumber and ω its frequency. To study the stability of the CWs (4.1), we add a small perturbation to the CW, so that the perturbed field

reads

$$A(z,t) = \Big[U(z) + \beta\,\sigma(z,t)\Big]e^{-i\omega t}, \qquad U(z) = a_s\,e^{iM_s z}, \tag{4.2}$$

where $\beta \ll a_s$ is a small parameter that measures the strength of the perturbation and $\sigma(z,t)$ is a weak noise. Substituting Eq. (4.2) into Eq. (2.1), using the stationary conditions (3.1)–(3.2), and keeping only the terms linear in σ and in its complex conjugate σ^*, we obtain the two coupled linear partial differential equations

$$\frac{\partial\sigma}{\partial t} = (1+i\nu)\frac{\partial^2\sigma}{\partial z^2} + (R+i\omega)\sigma - (1+i\mu)a_s^{2\gamma-2}\,\sigma - (1+i\mu)(\gamma-1)\,a_s^{2\gamma-2}(\sigma + e^{2iM_s z}\sigma^*), \tag{4.3}$$

$$\frac{\partial\sigma^*}{\partial t} = (1-i\nu)\frac{\partial^2\sigma^*}{\partial z^2} + (R-i\omega)\sigma^* - (1-i\mu)a_s^{2\gamma-2}\,\sigma^* - (1-i\mu)(\gamma-1)\,a_s^{2\gamma-2}(\sigma^* + e^{-2iM_s z}\sigma). \tag{4.4}$$

In Eqs. (4.3)–(4.4), the order of the nonlinearity enters through the factor $(\gamma-1)\,a_s^{2\gamma-2}$, which couples the noise σ to its complex conjugate σ^* and thus controls the exchange of energy between the CW and its modulation sidebands.

Since Eqs. (4.3) and (4.4) are linear, we look for normal-mode solutions of the form

$$\sigma(z,t) = B_1 \exp\big(-i\Omega z + \lambda t\big), \tag{4.5}$$

$$\sigma^*(z,t) = B_2 \exp\big(-i\Omega z + \lambda t\big), \tag{4.6}$$

where B_1 and B_2 are constant amplitudes, Ω is the modulation frequency, and λ is a complex eigenvalue whose real part is the temporal growth (or damping) rate of the perturbation and whose imaginary part is its frequency shift. Substituting Eqs. (4.5) and (4.6) into Eqs. (4.3) and (4.4) for the zero-wavenumber CW, $M_s = 0$, we obtain an eigenvalue problem for the noise amplitudes, which can be written in the 2×2 matrix form

$$\begin{pmatrix} i\lambda + Q & P \\ P^* & Q^* - i\lambda \end{pmatrix}\begin{pmatrix} B_1 \\ B_2 \end{pmatrix} = 0, \tag{4.7}$$

where

$$P = (i-\mu)(\gamma-1)\,a_s^{2\gamma-2},$$
$$Q = \omega - iR + (i-\nu)\Omega^2 + (i-\mu)a_s^{2\gamma-2} + P.$$

Non-trivial solutions of Eq. (4.7) require the determinant of the 2×2 matrix to vanish, which leads to the secular equation

$$\lambda^2 + 2\,\mathrm{Im}(Q)\,\lambda + |Q|^2 - |P|^2 = 0, \tag{4.8}$$

whose two roots are

$$\lambda = -\mathrm{Im}(Q) \pm \sqrt{|P|^2 - \big[\mathrm{Re}(Q)\big]^2}, \tag{4.9}$$

where

$$\mathrm{Re}(Q) = \omega - \nu\Omega^2 - \gamma\mu\,a_s^{2\gamma-2}, \quad \mathrm{Im}(Q) = \Omega^2 - R + \gamma\,a_s^{2\gamma-2} \quad \text{and} \quad |P|^2 = (1+\mu^2)(\gamma-1)^2 a_s^{4\gamma-4}.$$

The two eigenvalues are complex functions of the modulation frequency Ω. From the way λ was introduced in Eqs. (4.5) and (4.6), their imaginary parts give the dispersion relation of the perturbation, whereas their real parts give its temporal growth rate and therefore determine the stability of the CW amplitude a_s. Accordingly, the CW is neutrally (marginally) stable when $\mathrm{Re}[\lambda] = 0$, irrespective of the sign of $\mathrm{Im}[\lambda]$, unstable when $\mathrm{Re}[\lambda] > 0$ for at least one Ω, and asymptotically stable when $\mathrm{Re}[\lambda] < 0$ for all $\Omega \neq 0$, in which case the perturbed CW relaxes back

to its stationary state after a transient. Using this rule as a road map, we now explore the stability conditions of the CW regime. To begin with, Eq. (4.9) can be rewritten as

$$\lambda(\Omega) = -b - \Omega^2 \pm \sqrt{\Delta(\Omega)}, \qquad \Delta(\Omega) = b^2 - 2\nu\mu\, b\,\Omega^2 - \nu^2\Omega^4, \qquad b = (\gamma-1)R. \tag{4.10}$$

We first consider the limit of zero modulation frequency. Setting $\Omega = 0$ in the two eigenvalues (4.10), we obtain

$$\lambda_+ = 0, \qquad \lambda_- = -2(\gamma-1)R. \tag{4.11}$$

Since $\gamma > 1$ and $R > 0$, Eq. (4.11) shows that the CW regime is never unstable at zero modulation frequency: $\lambda_+ = 0$ is the neutral phase mode, associated with the invariance of Eq. (2.1) under a constant phase shift, and $\lambda_- < 0$ is the damped amplitude mode.

For a finite modulation frequency $\Omega \neq 0$, the stability is decided by the signs of the trace and of the determinant of the linear problem, which read

$$\mathrm{Tr} = -2\Big[(\gamma-1)R + \Omega^2\Big] < 0, \qquad \det = \Omega^2\Big[2(\gamma-1)R(1+\nu\mu) + (1+\nu^2)\Omega^2\Big]. \tag{4.12}$$

Because $\mathrm{Tr} < 0$ for all Ω, the CW is unstable if and only if $\det < 0$, which leads to the instability condition

$$2(\gamma-1)R(1+\nu\mu) + (1+\nu^2)\Omega^2 < 0 \iff \Omega^2 < -\frac{2(1+\nu\mu)(\gamma-1)R}{1+\nu^2} \equiv \Omega_c^2. \tag{4.13}$$

This condition can be fulfilled only if $\Omega_c^2 > 0$, i.e., only if $1 + \nu\mu < 0$, and the instability then occurs in the band $0 < \Omega < \Omega_c$. Condition (4.13) thus shows that the onset of MI depends only on the product $\nu\mu$ of the dispersive and nonlinear coefficients, and not on γ, whereas Ω_c plays the role of the cutoff frequency of the instability. Moreover, in Eq. (4.10), γ and R enter only through the combination $b = (\gamma-1)R$. Writing $\Omega^2 = b\,x$, one obtains

$$\lambda(\Omega) = b\,\Lambda(x), \qquad \Lambda(x) = -1 - x \pm \sqrt{1 - 2\nu\mu\, x - \nu^2 x^2}, \tag{4.14}$$

where Λ depends only on ν and μ. All the characteristic frequencies of the problem, namely Ω_{th}, Ω_c and $\Omega_{\max}$ introduced below, are therefore proportional to $\sqrt{b} = \sqrt{(\gamma-1)R}$, and all the growth rates, in particular $\mathrm{Re}(\lambda_+)_{\max}$, are proportional to b. For $\gamma = 2$ and $R = 1$, Λ is the growth rate of the modulations of the homogeneous oscillation ($Q = 0$) of the cubic CGL equation [1]. At the linear level, the zero-wavenumber CW of the generalized model thus behaves exactly as that of a cubic CGL equation with the effective gain $(\gamma-1)R$. The two eigenvalues coalesce at the modulation frequency at which $\Delta(\Omega)$ vanishes. For $\nu \neq 0$, this condition gives a quadratic equation in Ω^2:

$$\nu^2\Omega^4 + 2(\gamma-1)R\,\nu\mu\,\Omega^2 - (\gamma-1)^2R^2 = 0. \tag{4.15}$$

The reduced discriminant of Eq. (4.15) is $(\gamma-1)^2R^2\nu^2(1+\mu^2)$, which is strictly positive. Since $|\nu|\sqrt{1+\mu^2} > |\nu\mu|$, only one of the two roots is positive and thus physically relevant. This root defines the threshold frequency

$$\Omega_{th}^2 = \frac{(\gamma-1)R}{\nu^2}\Big[-\nu\mu + |\nu|\sqrt{1+\mu^2}\Big]. \tag{4.16}$$

Physically, Ω_{th} corresponds to the transition of the linearized dynamics from a node (real eigenvalues) to a focus (complex eigenvalues). This transition changes the nature of the relaxation of perturbations but not their stability, since the trace remains negative. The loss of stability of the CW is instead set by Ω_c, defined by $\det = 0$. At this point, a single real eigenvalue crosses zero, which corresponds to a stationary bifurcation of Benjamin–Feir type.

Figures 3 and 4 show the evolution of the real and imaginary parts, $\mathrm{Re}(\lambda)$ and $\mathrm{Im}(\lambda)$, of Eq. (4.9) as functions of the modulation frequency Ω, for $\gamma = 2, 3, 4, 5$, $R = 2$, $\nu = -0.5$ and

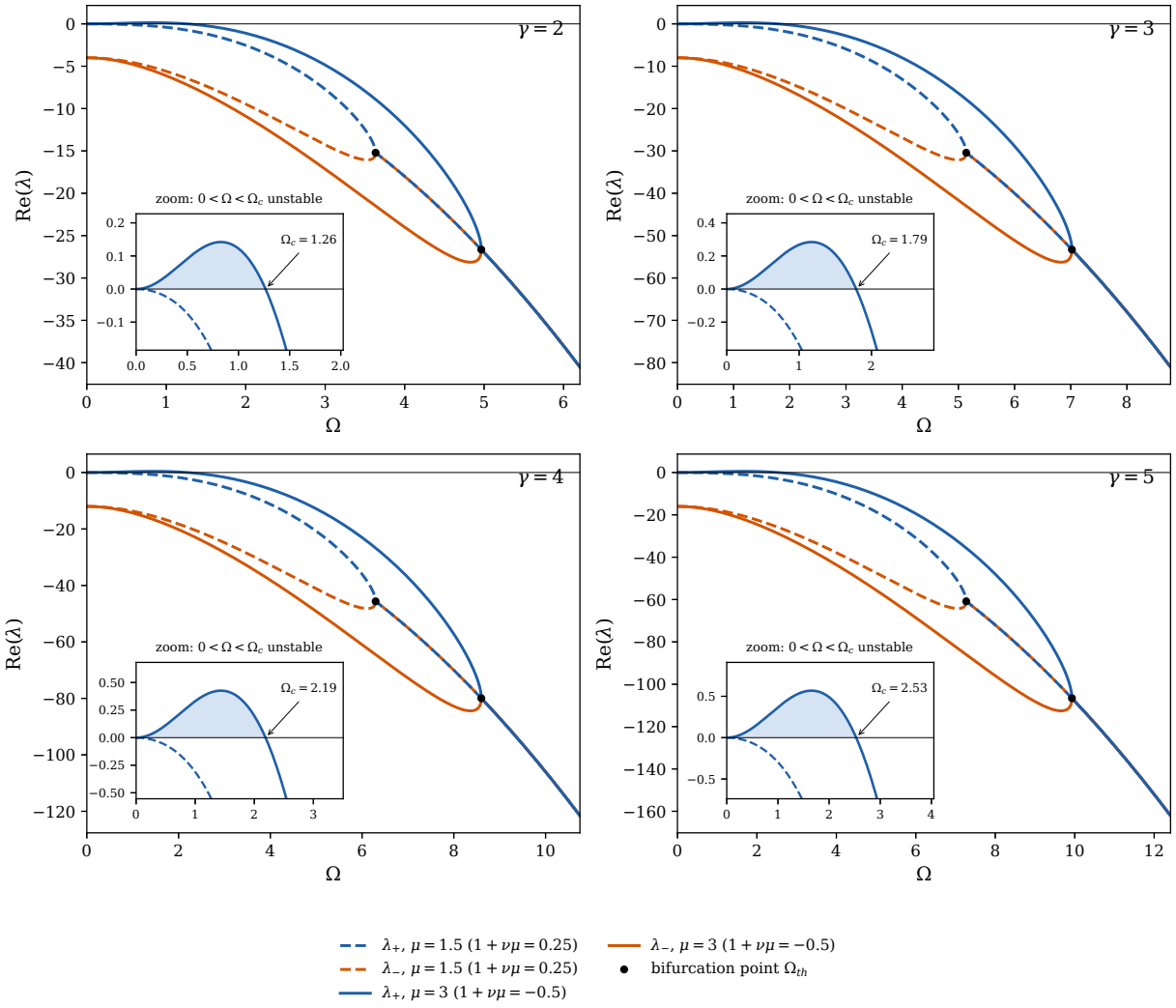


Figure 3: Growth rate $\mathrm{Re}(\lambda)$ versus modulation frequency Ω, Eq. (4.9), for $\gamma = 2, 3, 4, 5$, $R = 2$, $\nu = -0.5$, $\mu = 1.5$ (dashed) and $\mu = 3$ (solid). Blue: λ_+; orange: λ_-; black dots: bifurcation points Ω_{th}. The shaded vertical band is the unstable band $0 < \Omega < \Omega_c$ for $\mu = 3$, and the black square marks Ω_c, where the solid blue curve crosses zero. The maximum growth rate in this band, too small to be resolved at this scale, is given in each panel.

two nonlinear coefficients chosen on either side of the criterion: $\mu = 1.5$ $(1 + \nu\mu = 0.25 > 0)$ and $\mu = 3$ $(1 + \nu\mu = -0.5 < 0)$. For all the values of γ considered, the growth rate $\mathrm{Re}(\lambda)$ is a single-valued function that increases monotonically as the modulation frequency decreases, down to a bifurcation point Ω_{th} given by formula (4.16), where $\mathrm{Re}(\lambda)$ splits into two branches: the upper branch (blue curve) corresponds to the positive root λ_+, and the lower branch (orange curve) to the negative root λ_- in formula (4.9). Below Ω_{th}, the two roots are real and distinct: the upper branch λ_+ (blue) emerges from the neutral phase mode and the lower branch λ_- (orange) from the damped amplitude mode at $-2(\gamma - 1)R$. The branches merge at Ω_{th} (black dots), beyond which a single growth rate $-(\gamma - 1)R - \Omega^2$ remains and decreases quadratically, reflecting the dominance of spectral filtering at short modulation scales. Ω_{th} increases with μ for $\gamma = 2$ and, in accordance with Eq. (4.14), as $\sqrt{\gamma - 1}$ with the order of the nonlinearity. The sign of the upper branch at small Ω decides the stability of the CW. For $\mu = 1.5$, $\mathrm{Re}(\lambda_+) < 0$ for all $\Omega > 0$ and the CW is modulationally stable. For $\mu = 3$, $\mathrm{Re}(\lambda_+)$ is positive in the shaded band $0 < \Omega < \Omega_c$: long-wavelength modulations are amplified, with a maximum growth rate of 0.142 at $\Omega_{\max} = 0.828$ for $\gamma = 2$. Table 1 collects the characteristic values.

The positive lobe is small compared with the damping of the other modes, which is why it is

Table 1: Bifurcation point Ω_{th} [Eq. (4.16)], edge of the unstable band Ω_c [Eq. (4.13)] and maximum growth rate $\mathrm{Re}(\lambda_+)_{\max}$, reached at $\Omega_{\max}$, for $R = 2$ and $\nu = -0.5$. In accordance with Eq. (4.14), the frequencies for a given γ are those for $\gamma = 2$ multiplied by $\sqrt{\gamma - 1}$, and the growth rates are multiplied by $\gamma - 1$.

	$\mu = 1.5$ $(1 + \nu\mu = 0.25)$		$\mu = 3$ $(1 + \nu\mu = -0.5)$			
γ	Ω_{th}	$\mathrm{Re}(\lambda_+)_{\max}$	Ω_{th}	Ω_c	$\mathrm{Re}(\lambda_+)_{\max}$	$\Omega_{\max}$
2	3.635	0	4.965	1.265	0.142	0.828
3	5.140	0	7.021	1.789	0.284	1.172
4	6.295	0	8.599	2.191	0.426	1.435
5	7.269	0	9.930	2.530	0.569	1.657

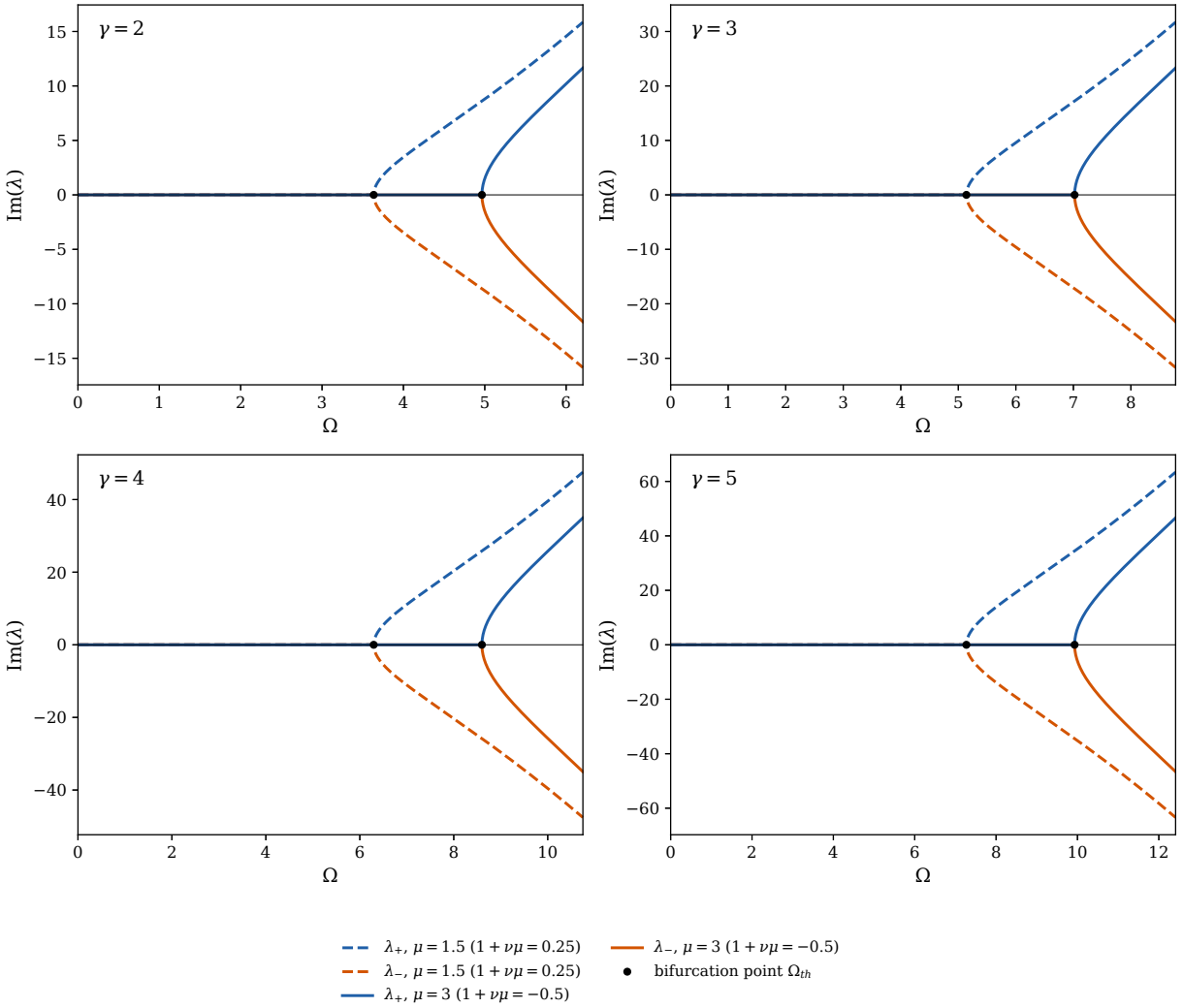


Figure 4: Frequency shift $\mathrm{Im}(\lambda)$ of the noise versus modulation frequency Ω, Eq. (4.9), for $\gamma = 2, 3, 4, 5$; $R = 2$, $\nu = -0.5$, $\mu = 1.5$ (dashed) and $\mu = 3$ (solid). Blue: λ_+; orange: λ_-; black dots: bifurcation points Ω_{th}.

hardly visible at the scale of Fig. 3; this weak, long-wavelength character is typical of Benjamin–Feir-type instabilities near threshold. When γ goes from 2 to 5, Ω_c increases from 1.265 to 2.530 and the maximum growth rate from 0.142 to 0.569, in exact agreement with the rescaling (4.14): a higher-order nonlinearity does not change whether the CW is unstable, but, by increasing the effective gain $(\gamma - 1)R$, it makes an unstable CW break up faster and into shorter modulation periods. In the focusing regime, the amplified modulation is expected to be reshaped by the

nonlinearity into a train of pulses with a period of the order of $2\pi/\Omega_{\max}$. Such instability-seeded pulse trains, with a repetition rate set by the gain band of the instability rather than by the cavity length, have been predicted [35] and observed in fibre lasers [36, 37]. Figure 4 complements this picture: $\mathrm{Im}(\lambda)$ vanishes identically for $\Omega < \Omega_{th}$, where $\Delta > 0$. At Ω_{th}, it splits into two branches $\pm\sqrt{-\Delta}$, which grow approximately as $|\nu|\Omega^2$ at large Ω, i.e., as the dispersive phase shift of the modulation. The two figures thus describe the same transition, from two real modes with different growth rates below Ω_{th} to a pair of oscillating modes with equal damping and opposite frequency shifts above it. Since the unstable band lies entirely below Ω_{th}, the growing perturbations are not frequency shifted: the instability amplifies a stationary modulation, locked in frequency to the CW. Because the unstable modes have no group velocity, the instability of the zero-wavenumber CW is absolute: the maximum of $\mathrm{Re}(\lambda_+)$ at the real frequency $\Omega_{\max}$ is a saddle point of $\lambda(\Omega)$ with a positive growth rate, so that a localized perturbation grows at a fixed position. This agrees with the cubic case, in which the plane waves with a small enough wavenumber are absolutely unstable beyond the Benjamin–Feir–Newell threshold [1].

4.2 Eckhaus instability of CWs with a nonzero wavenumber

The analysis above concerns the zero-wavenumber CW. To assess the stability of the CWs with $M_s \neq 0$, it is convenient to separate the perturbations of the amplitude and of the phase, and to write the perturbed field as

$$A(z,t) = \left[a_s + p(z,t) + i\,q(z,t)\right] e^{i(M_s z - \omega t)}, \tag{4.17}$$

where p and q are small real functions. Substituting Eq. (4.17) into Eq. (2.1), using the stationary conditions (3.1)–(3.2) and the first-order expansion $|A|^{2(\gamma-1)} \simeq a_s^{2\gamma-2}\left[1 + 2(\gamma-1)p/a_s\right]$, we obtain the linear system

$$\begin{cases} p_t = p_{zz} - \nu q_{zz} - 2M_s(q_z + \nu p_z) - 2b_s\, p, \\ q_t = q_{zz} + \nu p_{zz} + 2M_s(p_z - \nu q_z) - 2\mu b_s\, p, \end{cases} \tag{4.18}$$

with

$$b_s = (\gamma-1)\, a_s^{2\gamma-2} = (\gamma-1)(R - M_s^2). \tag{4.19}$$

The coefficient b_s is the coupling factor $(\gamma-1)a_s^{2\gamma-2}$ of Eqs. (4.3)–(4.4), evaluated on the locus (3.3). It is the only place where γ and R enter Eqs. (4.18), a property that underlies the mapping of Sec. 4.3. The terms proportional to M_s, which are absent for the zero-wavenumber CW, couple the amplitude and the phase through first-order derivatives; they are responsible both for the Eckhaus instability and for the drift of the perturbations.

Eigenvalue problem. We look for normal modes $(p,q) = (B_1, B_2)\exp(-i\Omega z + \lambda t)$, as in Eqs. (4.5)–(4.6). Since $\partial_z \to -i\Omega$ and $\partial_z^2 \to -\Omega^2$, Eqs. (4.18) reduce to

$$\begin{pmatrix} -\Omega^2 - 2b_s + 2i\nu M_s\Omega - \lambda & \nu\Omega^2 + 2iM_s\Omega \\ -\nu\Omega^2 - 2\mu b_s - 2iM_s\Omega & -\Omega^2 + 2i\nu M_s\Omega - \lambda \end{pmatrix} \begin{pmatrix} B_1 \\ B_2 \end{pmatrix} = 0. \tag{4.20}$$

Both diagonal elements contain the same imaginary term $2i\nu M_s\Omega$, which is a pure Doppler shift induced by the wavenumber of the CW. Setting $\lambda = 2i\nu M_s\Omega + \kappa$ removes it, and κ becomes an eigenvalue of the matrix

$$\mathbf{K} = \begin{pmatrix} -(\Omega^2 + 2b_s) & \nu\Omega^2 + 2iM_s\Omega \\ -(\nu\Omega^2 + 2\mu b_s) - 2iM_s\Omega & -\Omega^2 \end{pmatrix}, \tag{4.21}$$

whose trace and determinant are

$$\mathrm{Tr}\,\mathbf{K} = -2(\Omega^2 + b_s), \qquad \det\mathbf{K} = D_r + i\,D_i, \tag{4.22}$$

with

$$D_r = \Omega^2\Big[(1+\nu^2)\Omega^2 + 2b_s(1+\nu\mu) - 4M_s^2\Big], \qquad D_i = 4M_s\Omega(\nu\Omega^2 + \mu b_s). \tag{4.23}$$

Non-trivial solutions require $\det(\mathbf{K} - \kappa\mathbf{I}) = \kappa^2 - \kappa\,\mathrm{Tr}\,\mathbf{K} + \det\mathbf{K} = 0$, that is,

$$\kappa^2 + 2(\Omega^2 + b_s)\kappa + D_r + i\,D_i = 0. \tag{4.24}$$

For $M_s = 0$, one has $D_i = 0$ and $b_s = (\gamma-1)R$, and Eq. (4.24) reduces to the trace and the determinant of Sec. 4.1. The two eigenvalues are

$$\lambda_\pm = 2i\nu M_s\Omega - (\Omega^2 + b_s) \pm \sqrt{(\Omega^2+b_s)^2 - D_r - i\,D_i}. \tag{4.25}$$

At $\Omega = 0$, they reduce to $\lambda_+ = 0$ and $\lambda_- = -2b_s$: λ_+ is the branch connected to the neutral phase mode, and λ_- the branch connected to the damped amplitude mode. Writing $S = (\Omega^2+b_s)^2 - D_r$ and using $\mathrm{Re}\sqrt{S - iD_i} = \{[(S^2+D_i^2)^{1/2} + S]/2\}^{1/2}$, the Doppler term drops out of the real parts, which read

$$\mathrm{Re}(\lambda_\pm) = -(\Omega^2+b_s) \pm \sqrt{\frac{\sqrt{S^2+D_i^2}+S}{2}}. \tag{4.26}$$

Hence $\mathrm{Re}(\lambda_-) < 0$ for all Ω, and an instability can only occur through λ_+. The condition $\mathrm{Re}(\lambda_+) > 0$ is transformed as follows:

$$\begin{aligned}\mathrm{Re}(\lambda_+) > 0 &\iff \sqrt{S^2+D_i^2} > (\Omega^2+b_s)^2 + D_r \iff D_i^2 > 4(\Omega^2+b_s)^2 D_r,\\ &\iff (\Omega^2+b_s)^2\Big[(1+\nu^2)\Omega^2 + 2b_s(1+\nu\mu) - 4M_s^2\Big] < 4M_s^2(\nu\Omega^2+\mu b_s)^2,\end{aligned} \tag{4.27}$$

where the second equivalence follows by squaring (when the right-hand side of the first inequality is negative, $D_r < 0$ and both inequalities hold trivially), and the last one from Eq. (4.23) after division by $4\Omega^2$. Equation (4.27) is the exact instability condition of a CW of wavenumber M_s; it generalizes Eq. (4.13) to $M_s \neq 0$, and the edge Ω_E of the unstable band $0 < \Omega < \Omega_E$ is obtained by replacing the inequality with an equality. Since $\lambda_+(0) = 0$ as a consequence of the invariance of Eq. (2.1) under a constant phase shift, λ_+ is small for small Ω, and its sign is fixed by the first nonvanishing term of its expansion. A long-wavelength modulation is a slow variation of the local wavenumber, to which the amplitude, damped at the rate $2b_s$, adapts adiabatically. The Eckhaus instability is therefore a phase instability, which first appears in the limit $\Omega \to 0$: when a stability boundary is crossed, the band of unstable modes opens from $\Omega = 0$. Its onset is thus determined by the sign of the coefficient of Ω^2 in $\mathrm{Re}(\lambda_+)$. To obtain it, we write $\kappa_+ = c_1\Omega + c_2\Omega^2 + O(\Omega^3)$ and use $D_r = 2\Omega^2[b_s(1+\nu\mu) - 2M_s^2] + O(\Omega^4)$ and $D_i = 4\mu b_s M_s\Omega + O(\Omega^3)$ in Eq. (4.24). At order Ω, $2b_sc_1 + 4i\mu b_s M_s = 0$, i.e., $c_1 = -2i\mu M_s$; at order Ω^2, $c_1^2 + 2b_sc_2 + 2b_s(1+\nu\mu) - 4M_s^2 = 0$, i.e., $c_2 = 2(1+\mu^2)M_s^2/b_s - (1+\nu\mu)$. Adding the Doppler shift $2i\nu M_s\Omega$ gives

$$\mathrm{Re}(\lambda_+) = \left[\frac{2(1+\mu^2)M_s^2}{b_s} - (1+\nu\mu)\right]\Omega^2, \qquad \mathrm{Im}(\lambda_+) = -2(\mu-\nu)M_s\,\Omega. \tag{4.28}$$

Stability conditions. A CW is stable with respect to long-wavelength modulations if and only if the coefficient of Ω^2 in Eq. (4.28) is negative, i.e., $(1+\nu\mu)\,b_s > 2(1+\mu^2)M_s^2$. Three regimes follow. First, when $1+\nu\mu \leq 0$, the left-hand side is non-positive whereas the right-hand side is positive, so that every CW with $M_s \neq 0$ is unstable, whatever its wavenumber, the gain and the order γ; together with the result of Sec. 4.1 for $M_s = 0$, this shows that the Benjamin–Feir–Newell condition $1+\nu\mu < 0$ is the global instability threshold of all the CWs of the model. Second, when $1+\nu\mu > 0$, substituting $b_s = (\gamma-1)(R - M_s^2)$ gives the generalized Eckhaus criterion

$$M_s^2 < M_E^2 \equiv \frac{(\gamma-1)(1+\nu\mu)R}{2(1+\mu^2) + (\gamma-1)(1+\nu\mu)}, \tag{4.29}$$

or, equivalently, $a_s^{2\gamma-2} > R - M_E^2$. For $\gamma = 2$ and $R = 1$, Eq. (4.29) reduces to the classical Eckhaus criterion of the cubic equation [1], and it gives the explicit form, for a power-law nonlinearity, of the general plane-wave stability conditions of CGL-type equations [33]. Thus, only the CWs with $|M_s| < M_E$, which occupy the part of the locus (3.3) of Fig. 1 closest to the zero-wavenumber CW, are stable, whereas those with $M_E < |M_s| < \sqrt{R}$ are Eckhaus unstable. For all the parameter sets considered in this work, a scan of Eq. (4.27) over Ω shows that no instability appears at finite Ω when Eq. (4.29) is satisfied, so that Eq. (4.29) delimits the stable CWs. Third, unlike the zero-wavenumber case, the unstable perturbations are frequency shifted, since $\mathrm{Im}(\lambda_+) \neq 0$. With the convention $\exp(-i\Omega z + \lambda t)$, the growing modulation drifts along z with the group velocity

$$V_g = 2(\nu - \mu)M_s, \tag{4.30}$$

which does not depend on γ. For $\nu < \mu$, as in the present work, the modulations of the CW of wavenumber $+M_s$ drift toward $-z$, and those of the CW of wavenumber $-M_s$ toward $+z$. Because of this drift, the Eckhaus criterion is, strictly speaking, a criterion for convective instability; whether a localized perturbation also grows at a fixed position (absolute instability) is examined in Sec. 4.3. Because M_E^2 is proportional to R, Eq. (4.29) gives, in the plane $(1 + \nu\mu,\ M_s^2/R)$, a single curve for each γ, valid for any gain; this plane is shown in Fig. 5(a) for $\mu = 1.5$. The CWs lying below a curve are stable, those lying above it are Eckhaus unstable, and the stable band shrinks to zero at the Benjamin–Feir–Newell threshold $1 + \nu\mu = 0$ (vertical solid line), below which all the CWs are unstable (shaded region). At fixed $1 + \nu\mu > 0$, M_E^2/R increases with γ and tends to unity as γ get stronger; in the particular case $\nu = \mu$, it takes the simple form $M_E^2/R = (\gamma - 1)/(\gamma + 1)$, which grows from 1/3 for the Kerr nonlinearity. A higher-order nonlinearity thus widens the band of stable wavenumbers, because, at a given wavenumber, the coupling $b_s = (\gamma - 1)(R - M_s^2)$, which stabilizes the phase in Eq. (4.28), increases with γ. The vertical dotted line, $1 + \nu\mu = 0.25$, corresponds to the parameters $\nu = -0.5$ and $\mu = 1.5$ of Secs. 3 and 4.1, for which the zero-wavenumber CW is stable. Along this line, $M_E^2/R = 0.037$, 0.071, 0.103 and 0.133 for $\gamma = 2, 3, 4, 5$, so that only a small part of the loci of Fig. 1, close to $(a_0, 0)$, is stable. As $1 + \nu\mu = -1.25 < 0$, $P_\pm$ lie in the shaded region of Fig. 5(a) (cross) and are unstable for every γ.

Table 2: Eckhaus instability of the CWs $P_\pm = (a_s, 0, \pm M_s)$, for $R = 2$, $\nu = -1.5$, $\mu = 1.5$ and $\omega = -2$. C_2 is the long-wavelength coefficient in $\mathrm{Re}(\lambda_+) \simeq C_2\,\Omega^2$ [Eq. (4.28)], Ω_E the edge of the unstable band [Eq. (4.27)], and $\mathrm{Re}(\lambda_+)_{\max}$ the maximum growth rate, reached at $\Omega_{\max}$. $\mathrm{Re}\,\lambda_{\mathrm{abs}}$ is the absolute growth rate, i.e., the growth rate at a fixed position (Sec. 4.3).

γ	C_2	Ω_E	$\mathrm{Re}(\lambda_+)_{\max}$	$\Omega_{\max}$	$\mathrm{Re}\,\lambda_{\mathrm{abs}}$
2	33.75	2.450	1.374	1.262	1.373
3	17.50	2.316	1.194	1.155	1.179
4	12.08	2.191	1.152	1.053	1.077
5	9.38	2.097	1.180	1.041	1.030

Table 2 and Fig. 5(b) show that the instability of $P_\pm$ is much stronger than that of the zero-wavenumber CW of Table 1, obtained for the same gain $R = 2$: the maximum growth rate exceeds 1.15 for every γ, against 0.142 to 0.569 in Table 1. The long-wavelength coefficient $C_2 = 1.25 + 32.5/(\gamma - 1)$ is dominated by the term $2(1 + \mu^2)M_s^2/b_s$, which is large because a_s is small. The unstable band $0 < \Omega < \Omega_E$ narrows only slightly, from 2.450 to 2.097, when γ goes from 2 to 5, and the maximum growth rate depends weakly, and not monotonically, on γ: it decreases from 1.374 to 1.152 between $\gamma = 2$ and $\gamma = 4$ and increases again to 1.180 for $\gamma = 5$. Unlike the zero-wavenumber CW, whose growth rate scales exactly as $\gamma - 1$, the instability of these low-amplitude CWs is thus controlled mainly by their large wavenumber rather than by the order of the nonlinearity; the origin of this behaviour is explained in Sec. 4.3.

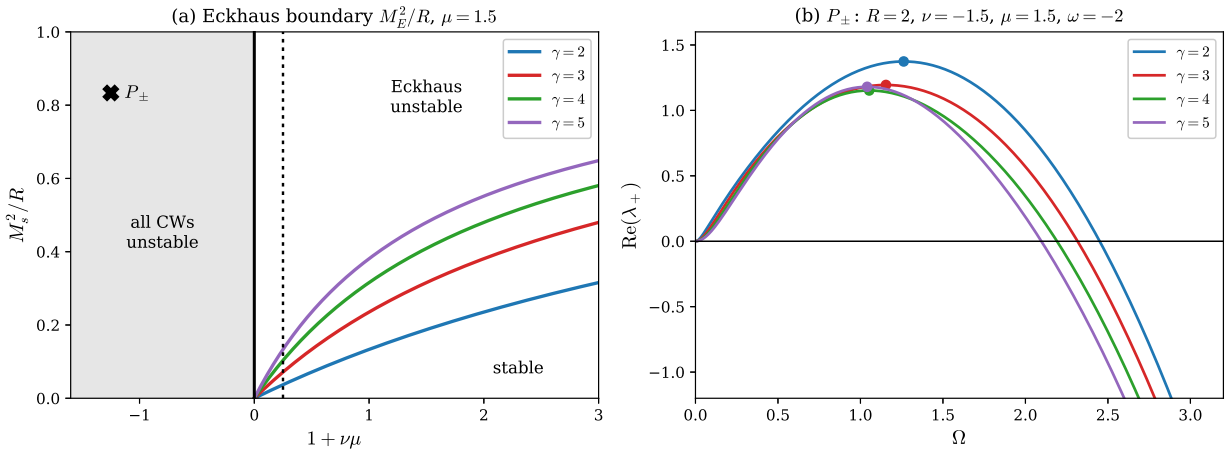


Figure 5: (a) Stability diagram of the CWs in the plane $(1+\nu\mu,\, M_s^2/R)$ for $\mu = 1.5$, valid for any gain R: Eckhaus boundary M_E^2/R [Eq. (4.29)] for $\gamma = 2, 3, 4, 5$. CWs below a curve are stable and CWs above it are Eckhaus unstable; in the shaded region $1+\nu\mu < 0$, bounded by the Benjamin–Feir–Newell threshold $1+\nu\mu = 0$ (vertical solid line), all the CWs are unstable. The vertical black dotted line, $1+\nu\mu = 0.25$, marks the parameters $\nu = -0.5$, $\mu = 1.5$ of Secs. 3 and 4.1; the cross marks the CWs $P_\pm$ ($1+\nu\mu = -1.25$, $M_s^2/R = 5/6$). (b) Growth rate $\mathrm{Re}(\lambda_+)$ versus Ω for the CWs $P_\pm$, for $R = 2$, $\nu = -1.5$, $\mu = 1.5$ and $\omega = -2$; filled circles: maxima $\mathrm{Re}(\lambda_+)_{\max}$ at $\Omega_{\max}$ (Table 2).

4.3 Role of the order γ in the linear stability and nature of the instability

Since Eqs. (4.18) depend on γ and R only through b_s, they coincide with the linearization of the cubic CGL equation $\partial_t A = R_{\rm eff} A + (1+i\nu)\partial_z^2 A - (1+i\mu)|A|^2 A$ about its plane wave of wavenumber M_s and squared amplitude $R_{\rm eff} - M_s^2 = b_s$, i.e., for

$$R_{\rm eff} = M_s^2 + (\gamma - 1)(R - M_s^2), \qquad Q_{\rm eff} = \frac{M_s}{\sqrt{R_{\rm eff}}}, \tag{4.31}$$

where $Q_{\rm eff}$ is the wavenumber in the units in which the effective gain equals unity. At the linear level, the order of the nonlinearity therefore acts only through an effective gain, which multiplies the growth rates, and an effective wavenumber. For the zero-wavenumber CW, $R_{\rm eff} = (\gamma-1)R$ and $Q_{\rm eff} = 0$, which is the rescaling (4.14). For the CWs $P_\pm$, with $R = 2$ and $M_s^2 = 5/3$, $R_{\rm eff} = (\gamma+4)/3$ and $Q_{\rm eff}^2 = 5/(\gamma+4)$: increasing γ raises the effective gain, from 2 to 3, but lowers the effective wavenumber, from $Q_{\rm eff}^2 = 0.833$ to 0.556, which brings the equivalent plane wave closer to the less unstable homogeneous state. The competition between these two effects explains the weak, non-monotonic γ-dependence of the growth rates in Table 2. Table 3 lists the main results of this work for arbitrary γ and R. For $\gamma = 2$ and a unit gain, $R = 1$, instead of the gain $R = 2$ used in the rest of this section, they reduce exactly to the known results for the cubic CGL equation, which provides a check of our calculations.

Considering the fact that the CWs with $M_s \neq 0$ drift with the group velocity (4.30), their instability may be only convective. We determined its nature in two independent ways: by locating the saddle point Ω_0 of the dispersion relation (4.25) in the complex Ω plane, $\partial\lambda/\partial\Omega = 0$ [38], and by integrating Eqs. (4.18) exactly in Fourier space for a localized Gaussian perturbation, on a domain large enough to avoid boundary effects, and measuring its growth at a fixed position. Both methods give the same absolute growth rates, $\mathrm{Re}\,\lambda(\Omega_0) \simeq 1.373$, 1.179, 1.077 and 1.030 for $\gamma = 2, 3, 4, 5$ (Table 2), so that $P_\pm$ are absolutely unstable for every γ. For $\gamma = 2$, the absolute growth rate practically coincides with the maximum growth rate, whereas for larger γ it is smaller, because part of the perturbation is advected toward $-z$, as expected from $V_g < 0$. The zero-wavenumber CW, which has no drift, is absolutely unstable whenever $1+\nu\mu < 0$ (Sec. 4.1). Consequently, $P_\pm$ cannot persist even in an open system, which motivates the search for non-CW stationary structures in Sec. 5.

Table 3: Main results of this work for arbitrary γ and R, their reduction to $\gamma = 2$ and $R = 1$, and the corresponding results of Aranson and Kramer [1] for the cubic CGL equation, with $b = \nu$, $c = \mu$, $Q = M_s$, $F = a_s$ and $b_s = (\gamma - 1)(R - M_s^2)$. Equation numbers in the last column refer to Ref. [1].

Quantity	This work (arbitrary γ, R)	This work ($\gamma = 2$, $R = 1$)	Ref. [1]
CW locus	$M_s^2 = R - a_s^{2\gamma-2}$, Eq. (3.3)	$M_s^2 = 1 - a_s^2$	$F^2 = 1 - Q^2$, Eq. (17)
CW dispersion relation	$\omega = \mu R + (\nu - \mu)M_s^2$, Eq. (3.6)	$\omega = \mu(1 - M_s^2) + \nu M_s^2$	$\omega = c(1 - Q^2) + bQ^2$, Eq. (17)
Stability of the $M_s = 0$ CW	$1 + \nu\mu > 0$, Eq. (4.13)	$1 + \nu\mu > 0$	$1 + bc > 0$ (Benjamin–Feir–Newell)
Determinant at $M_s = 0$	$\Omega^2[(1+\nu^2)\Omega^2 + 2(\gamma-1)R(1+\nu\mu)]$	$\Omega^2[(1+\nu^2)\Omega^2 + 2(1+\nu\mu)]$	Eq. (19) with $Q = 0$
Eckhaus boundary	$M_E^2 = \dfrac{(\gamma-1)(1+\nu\mu)R}{2(1+\mu^2)+(\gamma-1)(1+\nu\mu)}$, Eq. (4.29)	$M_E^2 = \dfrac{1+\nu\mu}{3+2\mu^2+\nu\mu}$	$Q_E^2 = \dfrac{1+bc}{3+2c^2+bc}$
Long-wavelength coefficient	$(1+\nu\mu) - \dfrac{2(1+\mu^2)M_s^2}{b_s}$, Eq. (4.28)	$(1+\nu\mu) - \dfrac{2(1+\mu^2)M_s^2}{1-M_s^2}$	$D_2 = 1 + bc - \dfrac{2(1+c^2)Q^2}{1-Q^2}$, Eq. (21)
Group velocity	$V_g = 2(\nu - \mu)M_s$, Eq. (4.30)	$V_g = 2(\nu - \mu)M_s$	$V_g = 2(b - c)Q$
Reduced dynamical system	Eq. (2.4)	Eq. (2.4) with $\gamma = 2$, $R = 1$	Eq. (33)

Summary and remarks

By carrying out a modulational-instability analysis of the zero-wavenumber CW and an Eckhaus-instability analysis of the CWs with a nonzero wavenumber M_s, we obtained the stability properties of the CWs of the model proposed in Sec. 2, for the gain $R = 2$. Both analyses are governed by the same Benjamin–Feir–Newell parameter $1+\nu\mu$, the zero-wavenumber case being recovered from the Eckhaus analysis in the limit $M_s \to 0$, and both reduce, for $\gamma = 2$ and $R = 1$, to the known results for the cubic CGL equation (Table 3). Their results can be summarized as follows:

- When $1 + \nu\mu > 0$, $\det > 0$ for all $\Omega \neq 0$: the two eigenvalues have a negative real part, and the zero-wavenumber CW is stable. This is the case $\mu = 1.5$, $\nu = -0.5$, with $1 + \nu\mu = 0.25$: $\mathrm{Re}(\lambda_+)_{\max} = 0$ in Table 1. The CWs with a nonzero wavenumber remain stable if and only if $M_s^2 < M_E^2$ [Eq. (4.29)], i.e., only the CWs closest to the zero-wavenumber CW share its stability. This band of stable wavenumbers widens with γ, since M_E^2/R increases with γ and tends to unity as $\gamma \to \infty$ [Fig. 5(a)].

- When $1 + \nu\mu < 0$, $\det < 0$ in the band $0 < \Omega < \Omega_c$, and the zero-wavenumber CW is unstable. This is the case $\mu = 3$, $\nu = -0.5$, with $1 + \nu\mu = -0.5$, in Table 1. The long-wavelength coefficient of Eq. (4.28) is then positive for every $M_s \neq 0$, so that every CW is unstable, whatever its wavenumber and the order γ. This is the case $\mu = 1.5$, $\nu = -1.5$, with $1 + \nu\mu = -1.25$, for the two CWs $P_\pm$ selected by $\omega = -2$ in Table 2 and Fig. 5(b).

The condition $1 + \nu\mu < 0$ is therefore the global instability threshold of all the CWs of the model, independently of γ. The order of the nonlinearity does not decide whether a CW is unstable, but how its instability develops, and, at the linear level, it does so only through the effective gain R_{eff} and the effective wavenumber Q_{eff} of Eq. (4.31). For the zero-wavenumber CW, the instability is stationary and absolute, and its cutoff frequency Ω_c and maximum growth rate scale exactly as $\sqrt{\gamma - 1}$ and $\gamma - 1$, as a consequence of this rescaling. For the CWs $P_\pm$, the instability is stronger, its growth rate depends only weakly on γ, and the unstable perturbations are frequency shifted and drift along z with the group velocity $V_g = 2(\nu - \mu)M_s$; these CWs are nevertheless absolutely unstable for every γ. In both cases, a CW cannot persist when $1 + \nu\mu < 0$, which motivates the search for the stationary multi-pulse structures of Sec. 5. The genuinely new effects of γ must therefore be sought in the nonlinear regime, which is not covered by the mapping.

5 Nonlinear regime: stationary and moving pulse trains

5.1 Stationary multi-pulse bursts ($v = 0$)

In the previous sections, we determined the singular solutions of the reduced system (2.4) and analysed the stability of the corresponding CWs. When a CW is coupled to a weak noise component,

the noise grows exponentially as soon as the real part of its amplification coefficient is positive. For the zero-wavenumber CW, this happens in the band $0 < \Omega < \Omega_c$ when the Benjamin–Feir–Newell condition $1 + \nu\mu < 0$ is fulfilled, and the growth rate increases with the order γ of the nonlinearity; under the same condition, all the CWs with a nonzero wavenumber are Eckhaus unstable (Sec. 4.2), and those considered below are absolutely unstable (Sec. 4.3). A CW therefore cannot persist, and the unstable field is expected to evolve, through modulational instability, into modulated structures such as pulse trains or multi-pulse structures. To obtain the profiles of the field amplitude a and of the instantaneous frequency M of these structures, we consider the stationary solutions ($v = 0$) of system (2.4). For $v = 0$, the coordinate $\tau = z - vt$ reduces to z, so that system (2.4) describes the spatial profiles of time-independent states: the evolution of (a, y, M) along τ is a spatial evolution along the propagation axis z, not a temporal one. Uniformly translating states, for which τ mixes space and time, are considered in Sec. 5.2. With $v = 0$, system (2.4) is also reversible, i.e., invariant under $(\tau, a, y, M) \to (-\tau, a, -y, -M)$. The three coupled nonlinear first-order equations for (a, y, M) are solved numerically with Luther's explicit sixth-order Runge–Kutta algorithm [34], with a fixed step $h = 10^{-4}$ over the interval $0 \le \tau \le 640$. The step must be small because the trajectories pass close to $a = 0$, where the factor $1/a$ in the equation for M' produces sharp variations. The most sensitive case is $\gamma = 2$: the integration diverges near $\tau \simeq 320$ with $h = 10^{-3}$, and departs from the converged trajectory after $\tau \simeq 321$ with $h = 5 \times 10^{-4}$ and after $\tau \simeq 420$ with $h = 2.5 \times 10^{-4}$, whereas $h = 1.25 \times 10^{-4}$, 10^{-4}, 6.25×10^{-5} and 3.125×10^{-5} give the same trajectory over the whole interval (to within 10^{-3} in a). For $\gamma = 3, 4, 5$, the trajectory is much less sensitive, and $h = 5 \times 10^{-4}$ already gives the converged trajectory.

The parameter values are $R = 2$, $\nu = -1.5$, $\mu = 1.5$, $\omega = -2$ and $\gamma = 2, 3, 4, 5$, i.e., the gain of Secs. 3 and 4. Note that ω is not the absolute optical frequency but a frequency (or propagation-constant) shift of the envelope A with respect to the carrier; it can therefore take negative values, which here originate from the dominant contribution $(\nu - \mu)M_s^2 < 0$ in Eq. (3.6). The frequency $\omega = -2$ lies inside the existence band (3.5), $-3 < \omega \le 3$, so that Eq. (3.4) provides two singular points of system (2.4), $P_\pm = (a_s,\, 0,\, \pm M_s)$, with $a_s^{2\gamma-2} = 1/3$, i.e., $a_s = 0.577$, 0.760, 0.833 and 0.872 for $\gamma = 2, 3, 4, 5$. They describe two CWs, $A = a_s\, e^{i(\pm M_s z - \omega t)}$, with the same amplitude a_s and the same frequency ω but opposite wavenumbers. P_+ is the CW whose phase increases along z ($M = +M_s = +1.291$), and P_- the CW whose phase decreases along z ($M = -M_s = -1.291$); they correspond to the two symmetric points $(a_s, \pm M_s)$ selected by the frequency ω on the locus of Fig. 1. Because ω lies close to the lower edge $\nu R = -3$ of the band, these CWs have a low amplitude and a large wavenumber, $M_s^2/R = 5/6$. Since $1 + \nu\mu = -1.25 < 0$, they are Eckhaus unstable for every γ (Table 2), and absolutely unstable (Sec. 4.3). In the phase space of system (2.4), $P_\pm$ are saddle-foci: the Jacobian matrix at P_- has one negative real eigenvalue, -0.228, -0.431, -0.611 and -0.768, and a pair of complex eigenvalues $\eta \pm i\varpi$ with $\eta = 0.114$, 0.216, 0.305, 0.384 and $\varpi = 2.639$, 2.705, 2.778, 2.852 for $\gamma = 2, 3, 4, 5$. A trajectory launched near $P_\pm$ therefore spirals away from it, with a spatial period $2\pi/\varpi \simeq 2.2$–2.4 and a growth rate η that increases with γ. The initial condition is taken close to P_- and is given by $(a,\, y,\, M)\big|_{\tau=0} = (0.8\, a_s,\, 0,\, -1.291)$, the negative sign of M indicating that the field is launched near the CW P_-. By reversibility, starting instead near P_+, with $(a, y, M)|_{\tau=0} = (0.8\, a_s,\, 0,\, +1.291)$, yields the same structure traversed in the opposite direction along τ, with M reversed in sign: the bursts, their peak amplitudes and their periods are unchanged.

Figure 6 shows the resulting profiles of the field amplitude $a(\tau)$ for $\gamma = 2, 3, 4, 5$, on a common vertical scale that allows a direct comparison of the four cases, and Table 4 collects their main characteristics. For all values of γ, the field does not remain on the unstable CW: starting from $0.8\, a_s$, the amplitude oscillates around a_s with a growing amplitude, as expected from the saddle-focus nature of $P_\pm$, and develops into a persistent multi-pulse structure along z. Each profile is a periodic alternation of a burst of fast pulses around a_s, with a spindle-shaped envelope, and a slow, nearly symmetric trough in which the amplitude falls almost to zero before recovering. The highest pulses and the deepest minima are both located at the center of each burst, so that the field is almost extinguished at the burst centres and at the trough bottoms. The order of the

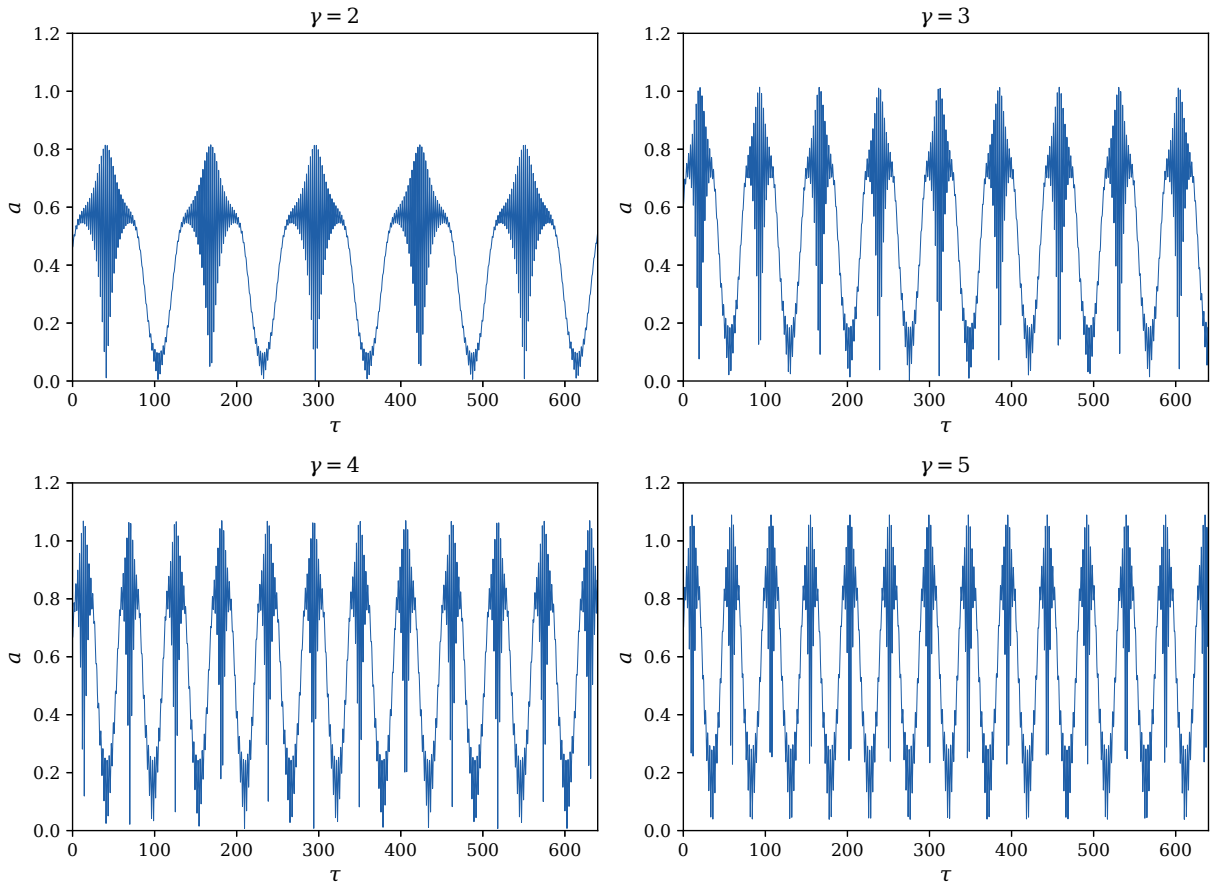


Figure 6: Multi-pulse profiles of the optical amplitude a along the spatial coordinate τ ($\tau = z$ for $v = 0$), obtained from numerical simulations of system (2.4) with $v = 0$. Parameter values are: $\gamma = 2, 3, 4, 5$; $R = 2$, $\nu = -1.5$, $\mu = 1.5$, $\omega = -2$.

Table 4: Characteristics of the multi-pulse profiles of Fig. 6 over $0 \leq \tau \leq 640$: amplitude a_0 of the zero-wavenumber CW, peak amplitude $a_{\max}$ of the pulses and ratio $a_{\max}/a_0$, number N_p of pulses above a_s per burst, mean spacing $\delta\tau$ between consecutive pulses inside a burst, spatial repetition period L of the bursts, range of the minima of a at the burst centres, and minimum and maximum values of M (Fig. 8).

γ	a_0	$a_{\max}$	$a_{\max}/a_0$	N_p	$\delta\tau$	L	$\min a$ at burst centres	$[M_{\min}, M_{\max}]$
2	1.414	0.815	0.58	26–27	2.38	126–129	0.002–0.053	[−133.7, 660.2]
3	1.189	1.014	0.85	13	2.33	72.6–74.9	0.018–0.127	[−106.9, 33.8]
4	1.122	1.070	0.95	9–10	2.28	55.5–57.8	0.007–0.202	[−196.3, 176.5]
5	1.091	1.090	1.00	7	2.24	48.1	0.229–0.261	[−9.1, 9.1]

nonlinearity acts on three features of these structures. First, the pulse peaks rise with γ, from 0.815 for $\gamma = 2$ to 1.014, 1.070 and 1.090 for $\gamma = 3, 4, 5$, so that on the common scale of Fig. 6 the tops of the bursts approach a nearly common level slightly above unity, whereas the saturation amplitude $a_0 = R^{1/(2\gamma-2)}$ decreases toward unity; the ratio $a_{\max}/a_0$ thus increases from 0.58 to 0.85, 0.95 and 1.00, so that the peaks are practically clamped at a_0 for $\gamma = 5$: for large γ, the power-law saturation $|A|^{2(\gamma-1)}$ is negligible for $a < a_0$ and dominant just above, and thus acts as an almost hard intensity limiter. Second, the bursts become shorter, contain fewer pulses (26–27, 13, 9–10 and 7) and repeat at shorter distances ($L \simeq 128$, 73, 56 and 48) as γ increases, whereas the spacing between consecutive pulses inside a burst remains almost unchanged ($\delta\tau = 2.38$ to 2.24). This spacing coincides with the period $2\pi/\varpi$ of the spiral motion around the saddle-foci $P_\pm$ (2.381, 2.322, 2.262 and 2.203), whereas the faster growth of this spiral, η, explains why the

bursts contain fewer pulses when γ increases. Third, the regularity of the bursts improves with γ: for $\gamma \leq 4$, the peak amplitude and the repetition period hardly change from one burst to the next, but the minima at the burst centres approach zero with a depth that varies from one cycle to the next (between 0.002 and 0.053 for $\gamma = 2$, and between 0.007 and 0.202 for $\gamma = 4$), and the number of pulses alternates for $\gamma = 2$ and $\gamma = 4$; for $\gamma = 5$, these minima remain far from zero (0.23–0.26), all the bursts contain seven pulses, the period is constant ($L = 48.1$) and successive cycles are nearly identical. A high-order nonlinearity therefore turns an irregular succession of long bursts into a regular, nearly periodic train of short bursts, whose peak amplitude is fixed by a_0 and whose spatial repetition period is tuned by γ.

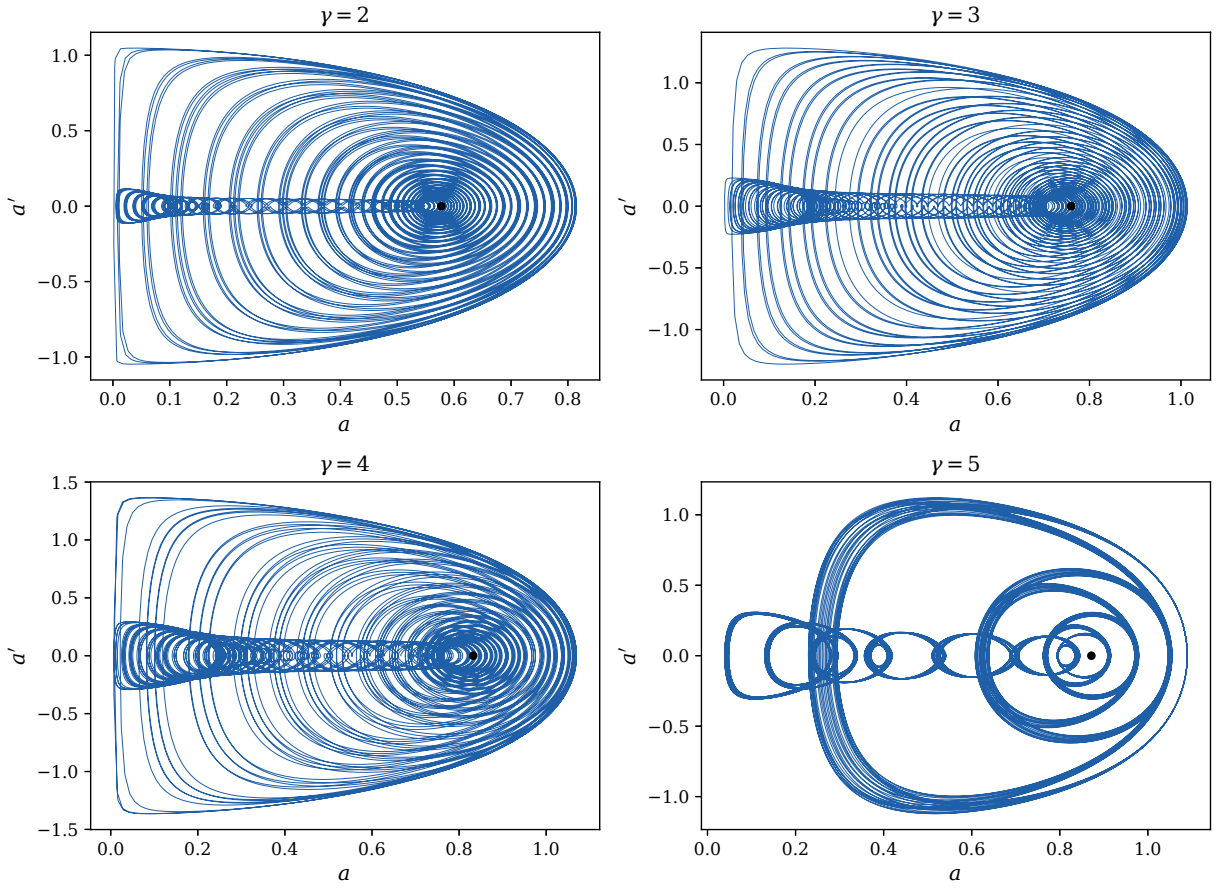


Figure 7: Phase portraits (a, a') of the optical amplitude, where the prime denotes the derivative with respect to τ, obtained from numerical simulations of system (2.4) for $\gamma = 2, 3, 4, 5$. Black dots: common projection $(a_s, 0)$ of the singular points $P_\pm$. Parameters as in Fig. 6.

A global picture of the profiles of Fig. 6 is given by the phase portraits of Fig. 7. The bursts appear as a family of nested loops around the common projection $(a_s, 0)$ of the two CWs, one loop per pulse, whose size follows the spindle-shaped envelope of the burst; the troughs appear as a narrow chain of small loops along the axis $a' \simeq 0$, extending from a_s down to almost zero. For $\gamma = 2, 3, 4$, the outer loops are rounded on the large-a side, where the peaks are limited by the nonlinear saturation, and almost vertical near $a = 0$, where the field passes through the sharp dips at the burst centres. Since the depth of these dips varies from one cycle to the next, successive bursts trace slightly different loops, which fill a dense bounded region whose extent in a' increases with γ, from $|a'| \simeq 1.05$ for $\gamma = 2$ to $|a'| \simeq 1.37$ for $\gamma = 4$. For $\gamma = 5$, the outer loops no longer reach $a = 0$, since they turn back at $a \simeq 0.23$, and the trajectory reduces to a few thin, well-separated bundles of loops that each cycle nearly retraces; the small loops of the trough remain confined between $a \simeq 0.04$ and a_s. Increasing γ thus changes the phase portrait from a dense family of nested loops to a discrete set of nearly closed curves, which confirms the transition from irregular

to nearly periodic bursts observed in Fig. 6.

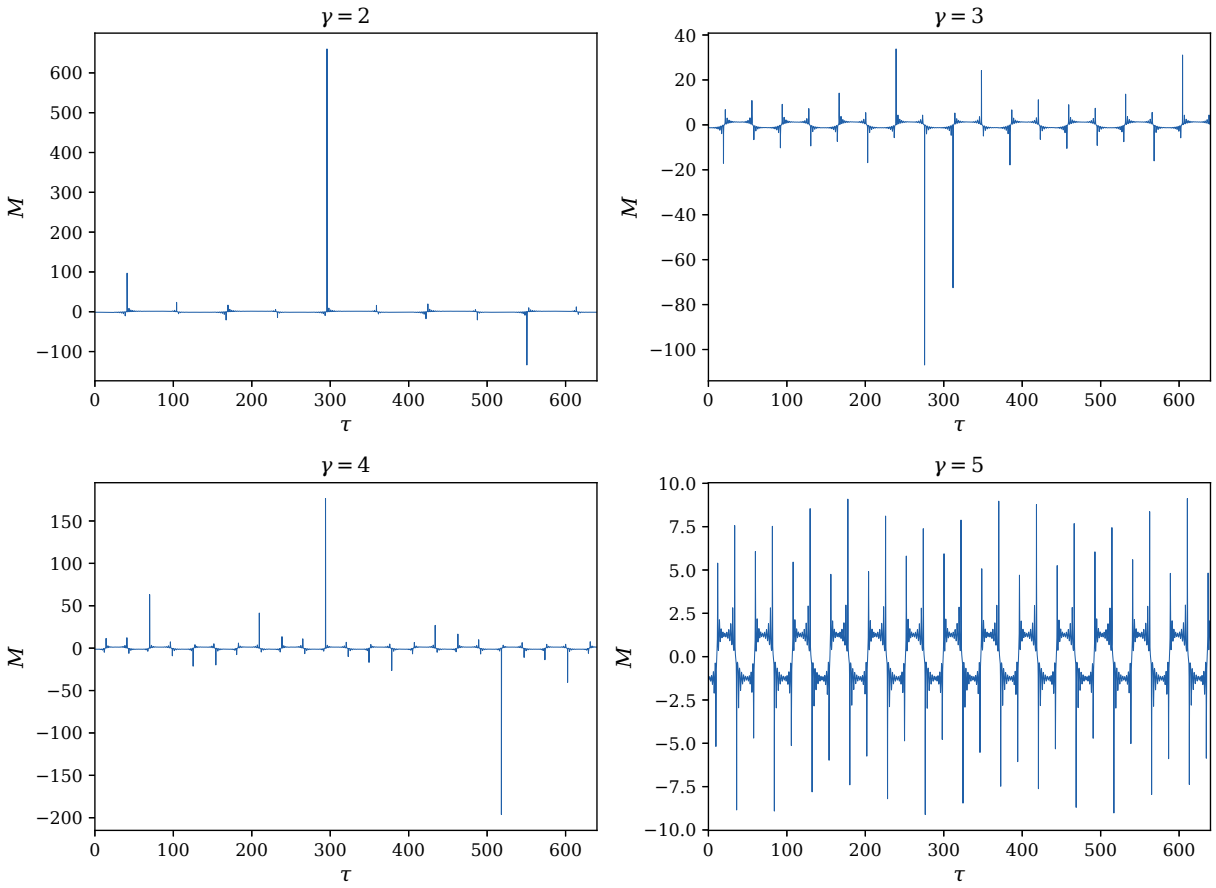


Figure 8: Profiles of the instantaneous frequency (local wavenumber) M along the spatial coordinate τ ($\tau = z$ for $v = 0$), obtained from numerical simulations of system (2.4) for $\gamma = 2, 3, 4, 5$. In each panel, the vertical axis covers the whole range of M over the simulated interval, from its minimum to its maximum value (Table 4). The large values of $|M|$ are reached at the phase slips, where a nearly vanishes. Parameters as in Figs. 6 and 7.

The instantaneous frequency $M(\tau)$, i.e., the local wavenumber of the field, which is the third variable of system (2.4), is plotted in Fig. 8 for $\gamma = 2, 3, 4, 5$, over its whole range of variation. For all values of γ, $M(\tau)$ remains most of the time on two plateaus close to the wavenumbers $-M_s = -1.291$ and $+M_s = +1.291$ of the two CWs selected by the common frequency ω, and switches from one plateau to the other twice per cycle: from $-M_s$ to $+M_s$ at each burst centre, and from $+M_s$ back to $-M_s$ at each trough bottom. Each switch is accompanied by a narrow spike of M, whose sign and height change from one switch to the next. For $\gamma = 2, 3, 4$, the vertical scale of Fig. 8 is set by a few isolated spikes of very large amplitude, so that the plateaus, of height ± 1.291, merge into a thin band around $M = 0$: for $\gamma = 2$, a single spike reaches $M = 660.2$ near $\tau \simeq 295$ and another one $M = -133.7$ near $\tau \simeq 550$, whereas all the other spikes remain below about 100 in absolute value; for $\gamma = 3$, the range is strongly asymmetric, $-106.9 \leq M \leq 33.8$, the largest spikes being negative; for $\gamma = 4$, it extends from -196.3 to 176.5. For $\gamma = 5$, in contrast, the range shrinks to $|M| \leq 9.1$, the two plateaus are directly visible, and every switch produces a spike of comparable height, between about 5 and 9 in absolute value, so that $M(\tau)$ displays sustained, approximately periodic oscillations. A change in the sign of M reverses the direction in which the phase Φ winds along z: on a plateau $M \simeq +M_s$, the phase increases along z, whereas on a plateau $M \simeq -M_s$, it decreases. Since the two plateaus have nearly the same length, the spatial average of M remains close to zero for all values of γ (between -0.013 and 0.026), despite the large amplitude of the individual spikes, so that no net phase gradient accumulates along z. The spikes

are located at the burst centres and at the trough bottoms, where a almost vanishes (Fig. 6). They originate from the factor $1/a$ in the equation for M' in system (2.4): when $a \to 0$, the phase of the field becomes ill defined, and Φ changes by a finite amount over a very short distance, which appears as a spike of $M = \Phi'$. These events are phase slips. Their height is set by the minimum value reached by a, which varies from one cycle to the next, and is therefore very sensitive to the trajectory; the extreme values of M (up to 660 for $\gamma = 2$) should thus be understood as markers of phase slips rather than as physically meaningful local wavenumbers. These regions are also the numerically most delicate parts of the integration, which is why a small integration step is required, as discussed above. As the nonlinearity exponent γ increases, the spikes are strongly reduced, although not monotonically, since the extreme values for $\gamma = 4$ (-196.3 and 176.5) exceed those for $\gamma = 3$ (-106.9 and 33.8). For $\gamma = 5$, the minima of a stay away from zero ($a \geq 0.039$), and the phase slips are replaced by moderate phase jumps. Taken together, these features point to a spatial switching dynamics between the two coexisting CW states of wavenumbers $\pm M_s$: the plateaus correspond to domains in which the field is locked on either state, while the burst centres and the trough bottoms, where the spikes of $M(\tau)$ occur, act as the walls between these domains. Within this picture, the nonlinearity exponent γ governs the nature of the switching process, which evolves from an intermittent regime dominated by isolated extreme phase slips for $\gamma = 2, 3, 4$ to a regular, quasi-periodic switching of moderate amplitude for $\gamma = 5$.

5.2 Moving pulse trains ($v \neq 0$)

In Sec. 5.1, the reduced system (2.4) with $v = 0$ showed that the unstable CWs $P_\pm$ develop into stationary multi-pulse bursts, irregular for $\gamma \leq 4$, along which the field switches between P_- and P_+ through phase slips. These bursts, however, are not periodic pulse trains, and, being time independent, they do not describe pulses that propagate. System (2.4) also contains the uniformly translating solutions $A(z,t) = a(\tau)\, e^{i[\Phi(\tau) - \omega t]}$, with $\tau = z - vt$ and $v \neq 0$, for which $|A(z,t)| = a(z - vt)$: a periodic orbit of system (2.4) with $v \neq 0$ is a train of identical pulses that moves at the constant velocity v, with a spatial period L equal to the period of the orbit and a temporal period $L/|v|$ at any fixed position. Since v enters the linearization of system (2.4) about its singular points, it can change the unstable spiral of P_- found in Sec. 5.1. Moreover, in the cubic CGL equation, the periodic orbits of the travelling-wave reduction are modulated amplitude waves, which organize the nonlinear development of the Eckhaus instability [22–24]. These two remarks motivate the case $v \neq 0$, which we now simulate. We integrate the same reduced system (2.4) as in Sec. 5.1, with the same explicit sixth-order Runge–Kutta algorithm of Luther [34], with a fixed step $h = 10^{-3}$ over the interval $0 \leq \tau \leq 200$, for the same parameters $R = 2$, $\nu = -1.5$, $\mu = 1.5$, $\omega = -2$ and $\gamma = 2, 3, 4, 5$, and for the velocity $v = 0.15$. The initial condition is $(a, y, M)|_{\tau=0} = (1.02\, a_*,\ 0,\ M_*)$, where $(a_*, 0, M_*)$ is the singular point of system (2.4) that continues P_- to $v \neq 0$, obtained by solving $y = 0$, $y' = 0$ and $M' = 0$ with Newton's method.

Figures 9–11 show that a nonzero velocity changes the nature of the structures obtained from the same unstable CW. In Fig. 9, the amplitude first oscillates around the singular point with a growing amplitude, as for $v = 0$, but this growth now saturates: after a short overshoot, the oscillation settles on a constant envelope, and the profile becomes a strictly periodic sequence of identical pulses, without bursts, troughs or modulation of the envelope. The transient becomes shorter as γ increases, because the spiral around the singular point grows faster for a higher-order nonlinearity, as already observed for the stationary bursts. The spacing between consecutive pulses is almost independent of γ and close to the spacing of the pulses inside the bursts of Fig. 6, since both are set by the frequency of the spiral motion around the singular point. For the same velocity, the minima of the pulses are practically the same for all γ, whereas their peaks rise with γ and approach the saturation amplitude a_0 of the zero-wavenumber CW: the pulses become higher and more contrasted, and their height is limited by the amplitude clamp of the power-law nonlinearity. The phase portraits of Fig. 10 make the mechanism explicit: the trajectory leaves the singular point along an expanding spiral and converges onto a single closed curve, a stable limit cycle that it then retraces indefinitely, instead of filling a dense region or a set of bundles as in Fig. 7. This

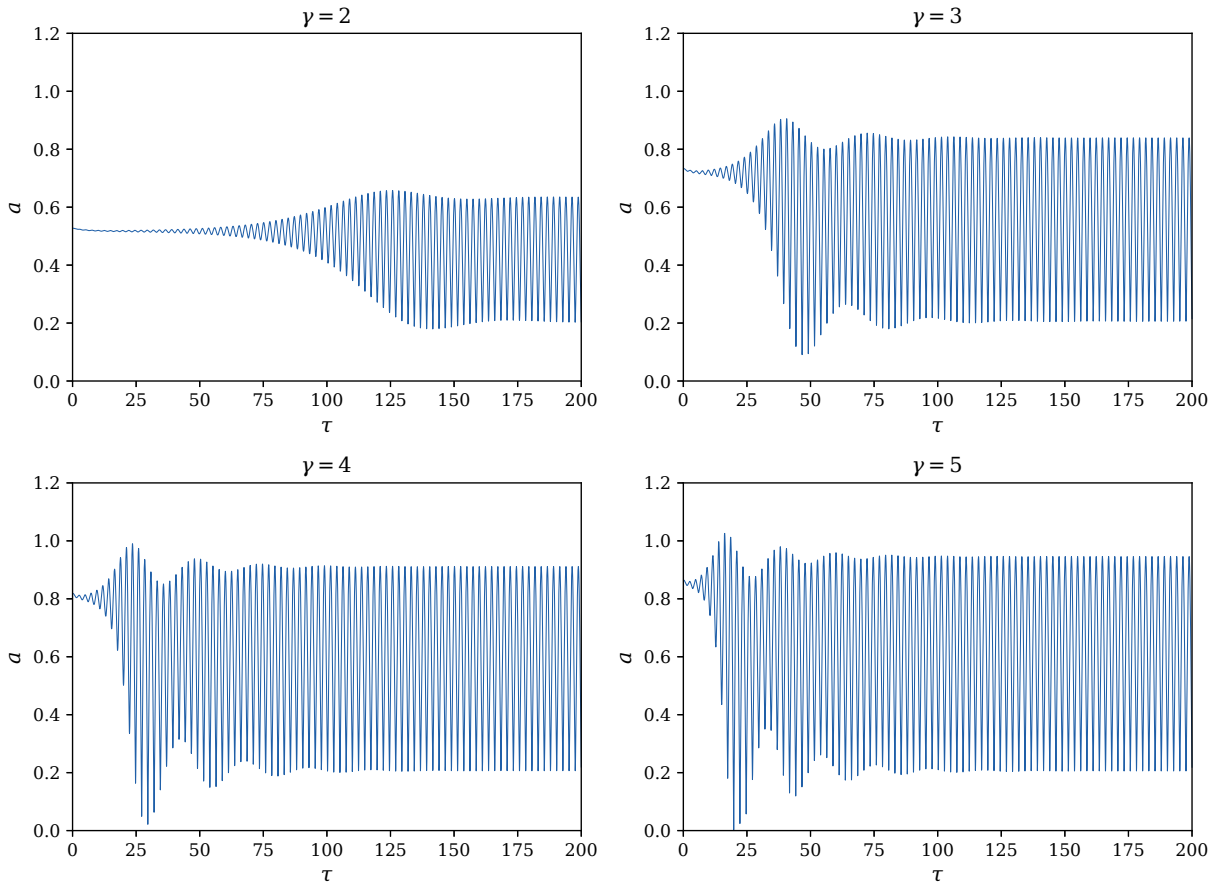


Figure 9: Amplitude profiles $a(\tau)$, $\tau = z - vt$, of the moving pulse trains obtained from numerical simulations of system (2.4) with $v = 0.15$, for $\gamma = 2, 3, 4, 5$. Parameters: $R = 2$, $\nu = -1.5$, $\mu = 1.5$, $\omega = -2$.

limit cycle surrounds the singular point, never reaches $a = 0$, and widens toward large amplitudes as γ increases. Figure 11 shows that the local wavenumber oscillates with the same period as the amplitude, its most negative values being reached at the minima of a and its least negative values close to its maxima, and that its excursions become larger as γ increases; above all, M never changes sign. Unlike the stationary profiles of Fig. 8, there is therefore no plateau at $+M_s$, no switching between the two CWs and no phase slip, since a never vanishes: the field remains locked on the CW P_-, and the pulses are a periodic modulation of this single CW. Since $\tau = z - vt$, each of these limit cycles corresponds to a train of identical pulses that moves rigidly along z at the velocity v and is periodic in time at any fixed position. A nonzero velocity therefore turns the irregular bursts of Sec. 5.1 into truly periodic moving pulse trains for every order of the nonlinearity.

Summary and remarks

In this section, the reduced system (2.4) was numerically solved with Luther's sixth-order Runge–Kutta scheme in the Benjamin–Feir–Newell unstable regime, for $R = 2$ and $\gamma = 2, 3, 4, 5$, starting near the unstable CW P_-. The main results can be summarized as follows.

- For $v = 0$ (Sec. 5.1), the singular points $P_\pm$ are saddle-foci with an unstable spiral, and the field develops into persistent stationary multi-pulse bursts separated by troughs. Along these structures, the field switches between the two CWs of opposite wavenumbers through phase slips located where the amplitude almost vanishes. Increasing γ clamps the pulse peaks near the saturation amplitude a_0, shortens the bursts, and turns an irregular succession of bursts with extreme phase slips into a regular, nearly periodic train of bursts with moderate phase jumps.

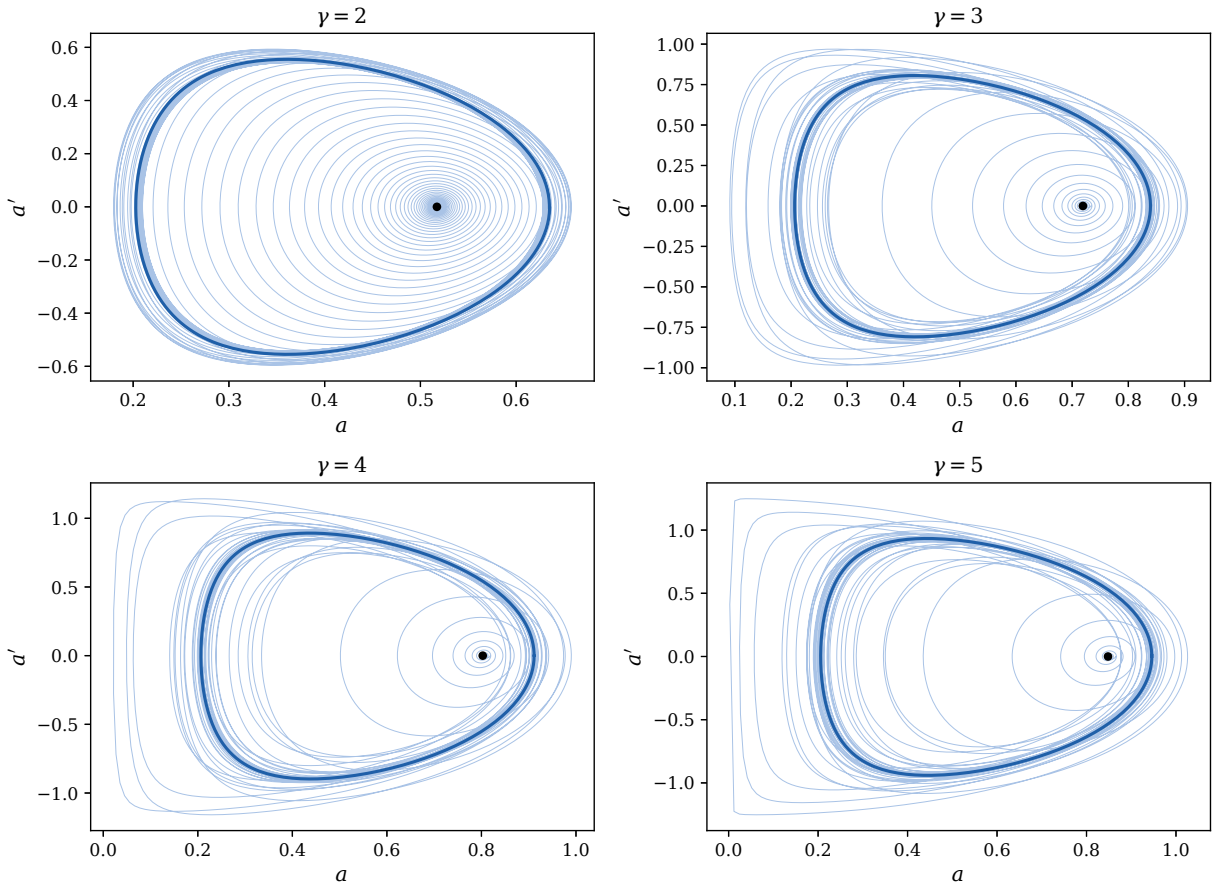


Figure 10: Phase portraits (a, a') of system (2.4) for $v = 0.15$ and $\gamma = 2, 3, 4, 5$. Light-blue curves: transient spiral; thick blue curves: limit cycle (one period of the periodic orbit); black dots: projection $(a_*, 0)$ of the singular point. Parameters as in Fig. 9.

- For $v \neq 0$ (Sec. 5.2), the same system and the same numerical scheme give a qualitatively different result: the growing spiral saturates on a stable limit cycle, and the field forms a strictly periodic train of identical pulses that moves at the constant velocity v and is periodic in time at a fixed position. The local wavenumber keeps a constant sign, so that these moving trains contain no phase slips and no switching between the two CWs.

- In both cases, the spacing between consecutive pulses is set by the frequency of the spiral motion around the singular point, and the order of the nonlinearity acts mainly through the amplitude clamp: a high-order nonlinearity raises the pulse peaks toward a_0, shortens the transients, and regularizes the dynamics.

The change of shape between Secs. 5.1 and 5.2 has a simple origin. For $v = 0$, system (2.4) is reversible, i.e., invariant under $(\tau, a, y, M) \to (-\tau, a, -y, -M)$; a reversible system has no attractors, so that the trajectory cannot settle on a cycle and wanders between the neighbourhoods of the two symmetric CWs $P_\pm$, which produces irregular bursts and phase slips. For $v \neq 0$, the terms proportional to v, in particular the friction-like term $-v\,y$ in the equation for y', break this reversibility and make the dynamics along τ dissipative: the trajectory can then be attracted by a limit cycle, which turns the bursts into a periodic train. The same terms break the equivalence between P_+ and P_-, since the transformation above now maps v onto $-v$: for $v > 0$, the cycle is born around P_-, whose modulations drift toward $+z$ with the group velocity $V_g = 2(\nu - \mu)M_s > 0$ (Sec. 4.2), i.e., in the direction of motion of the train. Because the amplitude stays away from zero along the cycle, the phase can never slip, and the local wavenumber M therefore keeps the negative sign of P_- along the whole train. Physically, the profiles of Sec. 5.1 are purely spatial, time-independent

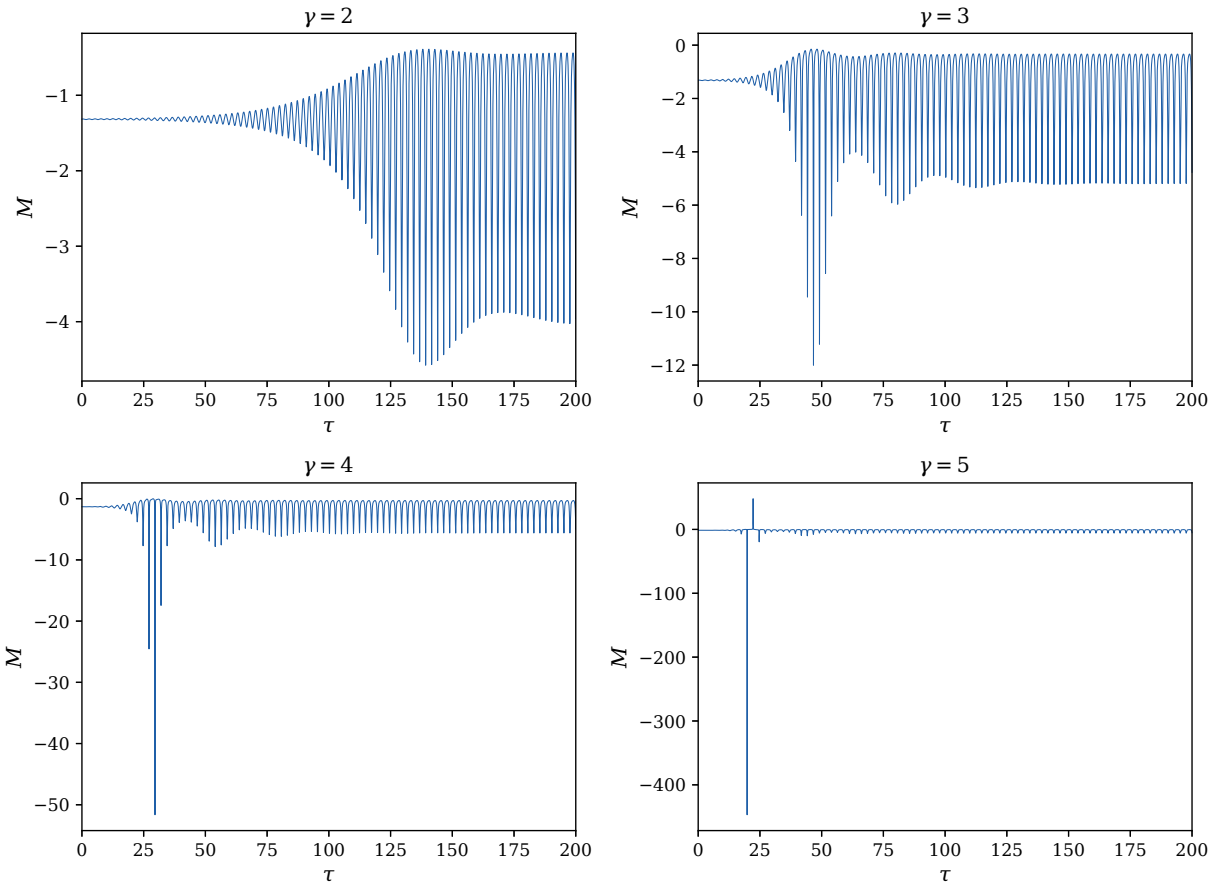


Figure 11: Profiles of the local wavenumber $M(\tau)$ obtained from numerical simulations of system (2.4) with $v = 0.15$, for $\gamma = 2, 3, 4, 5$. The vertical axis covers the whole range of M. Parameters as in Fig. 9.

patterns of the field along z, which describe stationary domains of the two CWs separated by phase defects, whereas, for $v \neq 0$, the variable $\tau = z - vt$ mixes space and time: the profile $a(\tau)$ is the spatial shape of the train in its own frame and, read at a fixed position z, it is also the temporal signal $a(z - vt)$ delivered by the medium, i.e., a periodic sequence of pulses of period $L/|v|$, as in the output of a mode-locked laser [5]. Such spatially periodic moving structures, obtained as limit cycles of the travelling-wave reduction of the complex Ginzburg–Landau equation, are known as modulated amplitude waves; they were shown to bifurcate from the uniform state through a Hopf bifurcation of the reduced system and to play a key role in the transition from phase to defect chaos in the cubic equation [22–24]. Our results show that this scenario persists for a power-law nonlinearity of arbitrary order γ.

Finally, the moving trains of Sec. 5.2 are exact uniformly translating solutions of Eq. (2.1), but their construction from the reduced system does not guarantee their stability in time. For the parameters considered here, for which $1 + \nu\mu < 0$ and the CWs $P_\pm$ are absolutely unstable (Sec. 4.3), direct integrations of Eq. (2.1) initialized with these trains show that they are destroyed by the Benjamin–Feir–Newell instability of the background CW. The search for parameters in which such periodic moving trains are also stable in time is a natural extension of this work.

6 Conclusion

We have studied a generalized complex Ginzburg–Landau equation with linear gain, spectral filtering, dispersion and a power-law nonlinearity of arbitrary order γ, in order to isolate the role of γ in the CW, modulational and pulsed regimes. A travelling-wave reduction showed that, for any γ, the CWs lie on the universal locus $M^2 = R - a^{2\gamma-2}$, inside a frequency band $\nu R < \omega \leq \mu R$ whose

edges do not depend on γ, and that high-order nonlinearities clamp the CW amplitudes close to unity. The linearized problem around any CW depends on γ only through the coupling coefficient $b_s = (\gamma - 1)(R - M_s^2)$, and it maps exactly onto that of a plane wave of the cubic equation with an effective gain R_{eff} and an effective wavenumber Q_{eff}. Consequently, the Benjamin–Feir–Newell condition $1 + \nu\mu < 0$ destabilizes all the CWs independently of γ, and the cutoff frequency and the maximum growth rate of the zero-wavenumber CW scale as $\sqrt{\gamma - 1}$ and $\gamma - 1$, respectively. For $1 + \nu\mu > 0$, the generalized Eckhaus criterion shows that the band of stable wavenumbers widens with γ, whereas the CWs $P_{\pm}$ used in the nonlinear analysis are absolutely unstable for every γ. For $\gamma = 2$ and $R = 1$, all these results reduce to the known ones for the cubic equation [1]. The order of the nonlinearity therefore decides how a CW becomes unstable, but not whether it does. In the nonlinear regime, numerical simulations of the reduced system with Luther's sixth-order Runge–Kutta scheme revealed two kinds of structures. For $v = 0$, the reduced system is reversible, and the unstable CWs develop into stationary multi-pulse bursts, along which the field switches between the two CWs of opposite wavenumbers through phase slips. For $v \neq 0$, reversibility is broken, and the trajectory settles on a stable limit cycle that describes a periodic train of identical pulses moving at a constant velocity without phase slips, i.e., a modulated amplitude wave [22, 23]. In both cases, increasing γ clamps the pulse peaks near the saturation amplitude a_0 and regularizes the dynamics, whereas the pulse spacing remains set by the frequency of the spiral motion around the singular point. Since these moving trains are unstable in time for the parameters considered here, a natural extension of this work is the search for parameter regions in which they are also stable in the full equation, as well as the inclusion of saturable absorption or higher-order dispersion.

Acknowledgments

The author thanks the German Academic Exchange Service (DAAD) for its financial support through the AIMS-Rwanda/Bielefeld University research cooperation. The author also thanks Bielefeld University in Germany, for its hospitality during a research visit, during which the numerical part of this work was carried out.

Funding

This paper is based on DAAD project, which received funding from the Federal Ministry of Research, Technology and Space.

Author contributions

P. Kameni Nteutse conceived the study, carried out the analytical and numerical work, analysed the results and wrote the manuscript.

Conflict of interest

The author declares no conflicts of interest.

Data availability

The data that support the findings of this study are available within the article.

References

[1] I. S. Aranson and L. Kramer, The world of the complex Ginzburg–Landau equation, Rev. Mod. Phys. **74**, 99–143 (2002).

[2] V. García-Morales and K. Krischer, The complex Ginzburg–Landau equation: an introduction, Contemp. Phys. **53**, 79–95 (2012).

[3] E. Kengne, W.-M. Liu, L. Q. English, and B. A. Malomed, Ginzburg–Landau models of nonlinear electric transmission networks, Phys. Rep. **982**, 1–124 (2022).

[4] N. Akhmediev and A. Ankiewicz (eds.), *Dissipative Solitons*, Lecture Notes in Physics, Vol. 661 (Springer, Berlin, 2005).

[5] Ph. Grelu and N. Akhmediev, Dissipative solitons for mode-locked lasers, Nat. Photonics **6**, 84–92 (2012).

[6] B. A. Malomed, Multidimensional dissipative solitons and solitary vortices, Chaos Solitons Fractals **163**, 112526 (2022).

[7] V. L. Kalashnikov, Chirped dissipative solitons of the complex cubic–quintic nonlinear Ginzburg–Landau equation, Phys. Rev. E **80**, 046606 (2009).

[8] N. Saha, B. Roy, and A. Khare, Higher-order complex cubic quintic Ginzburg–Landau equation: chirped solitary waves, EPL **142**, 20002 (2023).

[9] M. Mirzazadeh, M. Ekici, A. Sonmezoglu, M. Eslami, Q. Zhou, A. H. Kara, D. Milovic, F. B. Majid, A. Biswas, and M. Belić, Optical solitons with complex Ginzburg–Landau equation, Nonlinear Dyn. **85**, 1979–2016 (2016).

[10] İ. Önder, H. Esen, M. Özışık, A. Seçer, and M. Bayram, Optical soliton solutions of complex Ginzburg–Landau equation with triple power law and modulation instability, Opt. Quantum Electron. **56** (2024), doi:10.1007/s11082-024-06897-4.

[11] P. Kameni Nteutse, A. M. Dikandé, and S. Zekeng, Competing effects of Kerr nonlinearity and K-photon absorptions on continuous-wave laser inscriptions, Opt. Quantum Electron. **51**, 313 (2019).

[12] P. Kameni Nteutse, A. M. Dikandé, and S. Zekeng, Laser dynamics in nonlinear transparent media with electron plasma generation: effects of electron–hole radiative recombinations, J. Opt. **23**, 035402 (2021).

[13] E. O. Akeweje, G. Bader, A. M. Dikandé, and P. Kameni Nteutse, Femtosecond laser inscriptions in Kerr nonlinear transparent media: dynamics in the presence of K-photon absorptions, radiative recombinations and electron diffusions, J. Mod. Opt. **68**, 1211–1220 (2021).

[14] I. Ngek Ndifon and A. M. Dikandé, Modulational instability and nonlinear dynamics of femtosecond lasers in transparent materials with non-Kerr nonlinearities, AIP Adv. **13**, 075216 (2023).

[15] I. Ngek Ndifon and A. M. Dikandé, Dynamics of femtosecond lasers and induced plasma in non-Kerr nonlinear transparent materials: Competing effects of electron–hole radiative recombinations and single-electron diffusions, AIP Adv. **14**, 055320 (2024).

[16] C. R. Doering, J. D. Gibbon, and C. D. Levermore, Weak and strong solutions of the complex Ginzburg–Landau equation, Physica D **71**, 285–318 (1994).

[17] K. Hari, K. Manikandan, and R. Sankaranarayanan, Dissipative optical solitons in asymmetric Rosen–Morse potential, Phys. Lett. A **384**, 126104 (2020).

[18] T. J. Kippenberg, A. L. Gaeta, M. Lipson, and M. L. Gorodetsky, Dissipative Kerr solitons in optical microresonators, Science **361**, eaan8083 (2018).

[19] V. E. Zakharov and L. A. Ostrovsky, Modulation instability: the beginning, Physica D **238**, 540–548 (2009).

[20] J. M. Dudley, G. Genty, A. Mussot, A. Chabchoub, and F. Dias, Rogue waves and analogies in optics and oceanography, Nat. Rev. Phys. **1**, 675–689 (2019).

[21] G. van Baalen, Phase turbulence in the complex Ginzburg–Landau equation via Kuramoto–Sivashinsky phase dynamics, Commun. Math. Phys. **247**, 613–654 (2004).

[22] L. Brusch, M. G. Zimmermann, M. van Hecke, M. Bär, and A. Torcini, Modulated amplitude waves and the transition from phase to defect chaos, Phys. Rev. Lett. **85**, 86–89 (2000).

[23] L. Brusch, A. Torcini, M. van Hecke, M. G. Zimmermann, and M. Bär, Modulated amplitude waves and defect formation in the one-dimensional complex Ginzburg–Landau equation, Physica D **160**, 127–148 (2001).

[24] L. Brusch, A. Torcini, and M. Bär, Nonlinear analysis of the Eckhaus instability: modulated amplitude waves and phase chaos with nonzero average phase gradient, Physica D **174**, 152–167 (2003).

[25] J. M. Soto-Crespo, N. Akhmediev, and G. Town, Continuous-wave versus pulse regime in a passively mode-locked laser with a fast saturable absorber, J. Opt. Soc. Am. B **19**, 234–242 (2002).

[26] B. N. Aleksić, N. B. Aleksić, V. Skarka, and M. R. Belić, Modulation instability of solutions to the complex Ginzburg–Landau equation, Phys. Scr. **T162**, 014002 (2014).

[27] D. J. Fandio Jubgang, A. M. Dikandé, and A. Sunda-Meya, Continuous-wave stability and multipulse structures in a universal complex Ginzburg–Landau model for passively mode-locked lasers with a saturable absorber, J. Opt. Soc. Am. B **37**, A175–A183 (2020).

[28] B. B. Tchatchouang, I. Ngek Ndifon, A. M. Dikandé, and A. B. Moubissi, Soliton combs mediated by phonons and thermo-optic effects in Kerr optomechanical microresonators, Opt. Continuum **4**, 640–648 (2025).

[29] K. Nozaki and N. Bekki, Exact solutions of the generalized Ginzburg–Landau equation, J. Phys. Soc. Jpn. **53**, 1581–1582 (1984).

[30] W. van Saarloos and P. C. Hohenberg, Fronts, pulses, sources and sinks in generalized complex Ginzburg–Landau equations, Physica D **56**, 303–367 (1992).

[31] M. I. Carvalho, M. Facão, and O. Descalzi, Dissipative solitons onset through modulational instability of the cubic complex Ginzburg–Landau equation with nonlinear gradients, Chaos **35**, 093113 (2025).

[32] S. Correia and M. Figueira, A generalized complex Ginzburg–Landau equation: global existence and stability results, Commun. Pure Appl. Anal. (2021), doi:10.3934/cpaa.2021056.

[33] B. J. Matkowsky and V. Volpert, Stability of plane wave solutions of complex Ginzburg–Landau equations, Quart. Appl. Math. **51**, 265–281 (1993).

[34] H. A. Luther, An explicit sixth-order Runge–Kutta formula, Math. Comp. **22**, 434–436 (1968).

[35] A. M. Perego, N. Tarasov, D. V. Churkin, S. K. Turitsyn, and K. Staliunas, Pattern generation by dissipative parametric instability, Phys. Rev. Lett. **116**, 028701 (2016).

[36] N. Tarasov, A. M. Perego, D. V. Churkin, K. Staliunas, and S. K. Turitsyn, Mode-locking via dissipative Faraday instability, Nat. Commun. **7**, 12441 (2016).

[37] R. Si Fodil, F. Amrani, C. Yang, A. Kellou, and Ph. Grelu, Adjustable high-repetition-rate pulse trains in a passively-mode-locked fiber laser, Phys. Rev. A **94**, 013813 (2016).

[38] P. Huerre and P. A. Monkewitz, Local and global instabilities in spatially developing flows, Annu. Rev. Fluid Mech. **22**, 473–537 (1990).